Superfluid drag of two-species Bose-Einstein condensates in optical lattices

Patrick P. Hofer

Departement of Physics

University of Basel

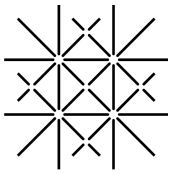

Masters thesis under the supervision of

Dr. Vladimir M. Stojanović

in the group of

Prof. Dr. Christoph Bruder

November, 2012

Abstract

We investigate the superfluid drag that occurs between the components of a two-species Bose-Einstein condensate in quasi two-dimensional optical lattices. This drag couples the two different superfluid velocities in the free energy, which are used to describe such a system. We derive an analytic expression of the drag in the limit of weak interactions by solving the Bose-Hubbard Hamiltonian in the Bogoliubov approximation and subsequent expansion of the free energy in the superfluid velocities. This expression is evaluated numerically for different lattice geometries by calculating the bandstructures and Bose-Hubbard interaction parameters using a plane-wave expansion of the single-particle Hamiltonian. The numerical approach allows us to investigate shallow optical lattices, where to our knowledge the superfluid drag has so far not been studied.

Although quantitatively the superfluid drag varies with the lattice geometry, we find its qualitative behavior to be very general. The drag shows a non-monotonic dependence on the lattice depth, which is the result of two competing effects: when increasing the lattice depth, the drag is enhanced by the increase in the interspecies interaction energy while at the same time it is reduced by the decrease in the kinetic energy. Furthermore, we found the mass ratio which maximizes the drag to be dependent on the lattice depth, a result which is in contradiction to previous findings in the literature.

Contents

Chapter 1

Introduction

At temperatures below $1\,\mu$K, an ensemble of atoms is termed ultracold and its behavior is predominantly determined by quantum-statistical effects. The experimental realization of a gas of ultracold atoms therefore allows for the investigation of a macroscopic number of particles, whose behavior is determined by quantum mechanics. In such a system, the collective quantum behavior appears in the phenomena of Bose-Einstein condensation (BEC) and superfluidity [1].

The manifestation of the underlying statistics is of course heavily dependent on the environment imposed by any external potential such as an optical lattice. In this case, the potential is created by interfering laser beams. The resulting intensity landscape imposes a potential landscape on the atoms via the Stark shift. Optical lattices have many favorable features such as the absence of defects and the ability to dynamically control relevant parameters; therefore they constitute a versatile tool for controlling the properties of ultracold atomic gases [2].

In this work, we study the phenomenon of superfluid drag in optical lattices, an effect that occurs in a two-component superfluid. In the continuum, this effect was first investigated by Andreev and Bashkin in the context of ^{3}He-^{4}He mixtures [3]. They found, that the motion of one superfluid component drags along the second component in a dissipationless fashion. Although a microscopic theory of the drag between two weakly interacting Bose gases was developed in the continuum limit [4], there is not much literature on superfluid drag in optical lattices. For the special case of the three-dimensional cubic lattice, the drag was investigated in the framework of the tight-binding approximation by Linder and Sudbø [5]. Just recently, the superfluid drag of weakly interacting bosons was investigated in n-dimensional cubic lattices and the obtained results qualitatively agree with ours [6]. For a system of strongly interacting bosons, the superfluid drag was investigated by means of Monte Carlo simulations [7].

Our goal was to generalize the work of Linder and Sudbø [5] to different lattice geometries and to shallow optical lattices. In particular, we derive an expression for the superfluid-drag coefficient valid for an arbitrary lattice, which is then evaluated numerically for different lattice geometries. This derivation proceeds by diagonalizing the Bose-Hubbard Hamiltonian that describes a two-component BEC in an optical

lattice using the Bogoliubov approximation. The superfluid-drag coefficient can then be derived by expanding the free energy in the superfluid velocities. The resulting expression depends on the bandstructures and the Hubbard-interaction parameters which are obtained numerically by means of a truncated plane-wave expansion of the single-particle Hamiltonian. Using this numerically exact approach, instead of the tight-binding approximation, we obtain results that are reliable even in the limit of shallow optical lattices, where superfluidity is assured for both commensurate and incommensurate filling.

As a result of the interplay between the interaction and kinetic energies, we find a non-monotonic dependence of the superfluid-drag coefficient on the optical lattice depth. In contrast to Ref. 5, where the mass ratio which maximizes the superfluid drag was found to be around unity for an arbitrary lattice depth, we find that the optimal mass ratio depends on the lattice depth.

In addition to the two-dimensional square lattice, we investigate the drag in the particularly interesting three-beam lattices (3BLs). These are two-dimensional optical lattices created by three in-plane laser beams [8]. One special case of 3BLs is the triangular optical lattice, which has lately received attention in connection with the experimental observation of the transition from a superfluid to a Mott-insulator (SF-MI) [9].

The thesis is organized as follows, the remainder of this chapter provides the background knowledge. In Sec. 1.1, BEC is discussed, Sec. 1.2 gives an introduction to superfluidity and superfluid drag, in Sec. 1.3 we discuss some general principles of ultracold atoms, Sec. 1.4 introduces the optical lattices which provide the environment where we investigate the superfluid drag, in Sec. 1.5 we discuss some basic properties of the Bose-Hubbard model which is used to describe ultracold atoms in optical lattices and in Sec. 1.6 we give a short overview of the experimental progress that has been made towards the observation of the superfluid drag. In Ch. 2 and 3 we present the actual work we have done. Chapter 2 gives a derivation of an expression for the superfluid-drag coefficient, which is valid for an arbitrary lattice geometry, and Ch. 3 is devoted to the numerical evaluation of this expression. We present our results in Ch. 4 and, finally, conclude in Ch. 5.

A more condensed form of our findings is published and can be found in Ref. 10.

For convenience we set $\hbar = 1$ throughout this thesis.

1.1 Bose-Einstein condensation

BEC was predicted by Albert Einstein in 1924, based on ideas developed by Satyendra Nath Bose. In a system of bosons, below the transition temperature, a macroscopic fraction of the particles occupy a single-particle state. The quantum mechanical properties of this state, which are usually too small to have any noticeable effect, are therefore amplified in a BEC and can be made visible.

1.1.1 Definition

A definition of BEC can be given in terms of the single-particle reduced density matrix ρ_1. In terms of the boson field operators $\psi(\boldsymbol{r})$ [$\psi^\dagger(\boldsymbol{r})$], which annihilate [create] a boson at position $\boldsymbol{r}$, its matrix elements are given by

$$g(\boldsymbol{r},\boldsymbol{r}') \equiv \langle \boldsymbol{r}'|\rho_1|\boldsymbol{r}\rangle \equiv \langle \psi^\dagger(\boldsymbol{r})\psi(\boldsymbol{r}')\rangle. \tag{1.1}$$

The last expression shows, that ρ_1 is a hermitian operator and can therefore be diagonalized with real eigenvalues

$$g(\boldsymbol{r},\boldsymbol{r}') = \sum_i \langle \boldsymbol{r}'|\chi_i\rangle \langle\chi_i|\rho_1|\chi_i\rangle \langle\chi_i|\boldsymbol{r}\rangle = \sum_i N_i \chi_i^*(\boldsymbol{r})\chi_i(\boldsymbol{r}'), \tag{1.2}$$

where $|\chi_i\rangle$ denote the eigenstates of the single-particle reduced density matrix and its eigenvalues fulfill the condition $\sum_i N_i = N$, N being the total number of particles. A system shows BEC if there is one extensive eigenvalue N_0 of order N, while all the others are of order one. The macroscopically occupied single-particle state is then given by $\chi_0(\boldsymbol{r})$.

1.1.2 The order parameter

To describe BEC and the closely related superfluid phase, it is convenient to introduce an order parameter $\Psi(\boldsymbol{r})$ which steadily rises from zero below the critical temperature. The simplest definition of the order parameter is given in terms of the extensive eigenvalue of the single-particle reduced density matrix and the corresponding eigenstate

$$\Psi(\boldsymbol{r}) = \sqrt{N_0}\chi_0(\boldsymbol{r}) = \sqrt{n_0(\boldsymbol{r})}e^{i\phi(\boldsymbol{r})}, \tag{1.3}$$

with $\int d\boldsymbol{r}\, n_0(\boldsymbol{r}) = N_0$.

Based on the idea of spontaneously broken gauge symmetry, another definition that is widely used in the literature can be motivated by the concept of off-diagonal long range order (ODLRO). In a translation invariant system, the eigenfunctions of the single-particle reduced density matrix are plane waves and its matrix elements read

$$g(\boldsymbol{r}-\boldsymbol{r}') = \langle \psi^\dagger(\boldsymbol{r})\psi(\boldsymbol{r}')\rangle = n_0 + {\sum_{\boldsymbol{k}}}' n_{\boldsymbol{k}} e^{-i\boldsymbol{k}(\boldsymbol{r}-\boldsymbol{r}')}, \tag{1.4}$$

where $n_{\boldsymbol{k}} = N_{\boldsymbol{k}}/\mathcal{V}$ are the occupation numbers in $\boldsymbol{k}$-space divided by the system volume. When taking the limit $\left|\boldsymbol{r}-\boldsymbol{r}'\right| \to \infty$, the matrix element therefore converges to the value n_0 which is non-zero in a BEC and the system is said to exhibit ODLRO. In this limit, it seams plausible to treat the points $\boldsymbol{r}$ and $\boldsymbol{r}'$ as statistically independent and the above average reduces to the product of two independent averages which we can identify as the order parameter

$$\begin{aligned} &\langle \psi^\dagger(\boldsymbol{r})\rangle\langle\psi(\boldsymbol{r}')\rangle = n_0, \\ &\Psi(\boldsymbol{r}) \equiv \langle\psi(\boldsymbol{r})\rangle = \sqrt{n_0(\boldsymbol{r})}e^{i\phi(\boldsymbol{r})}. \end{aligned} \tag{1.5}$$

In the second equation we have reintroduced the space dependence of n_0 to generalize the order parameter to the non-translational invariant case. In a lattice, the plane waves have to be replaced by Bloch waves. Consequently $g(\boldsymbol{r}, \boldsymbol{r}')$ oscillates around a non-zero value as one takes the limit $\left|\boldsymbol{r} - \boldsymbol{r}'\right| \to \infty$ and the order parameter can be defined as in the last expression.

To obtain a value other than zero, the above averages have to be taken over an ensemble which respects the broken gauge symmetry. As in a ferromagnet, where the rotational invariance is spontaneously broken, the ergodic hypothesis does not hold anymore. Whereas in a ferromagnet one has to restrict oneself to states in which the magnetization has small deviations from a preferred direction, in a superfluid the ensemble only contains states with small deviations from a preferred phase field $\phi(\boldsymbol{r})$, which is connected to the superfluid flow pattern [11].

Motivated by single-particle wave mechanics, one can define a condensate density and velocity

$$\begin{aligned} \rho_c(\boldsymbol{r}) &= |\Psi(\boldsymbol{r})|^2, \\ \boldsymbol{v}_s(\boldsymbol{r}) &= \frac{1}{m}\boldsymbol{\nabla}\phi(\boldsymbol{r}). \end{aligned} \tag{1.6}$$

Note that the condensate density is not equal to the superfluid density but the condensate velocity is the same as the superfluid velocity [12]. The superfluid density and velocity and their interpretations are discussed in more detail in the next chapter.

1.2 Superfluidity

The term superfluidity stands for a complex of phenomena, including lack of viscosity and the support of heat waves, which occur in some substances below a critical temperature ($T \lesssim 2.17$ K for ^{4}He). Although its relation to BEC is still a subject of debate, the two phenomena are closely related and can in many cases be interpreted as two sides of the same coin.

1.2.1 The one-component superfluid

A phenomenological description of the superfluid state is given by the "two-fluid" model which describes the system as a mixture of a superfluid part, flowing dissipationless, and a normal part, which behaves as an ordinary liquid [13]. The two parts do not exchange momentum and are characterized by their densities ρ_s, ρ_n, with the total mass density being their sum, and velocities $\boldsymbol{v}_s$, $\boldsymbol{v}_n$. The connection to BEC is given by the above definition of the superfluid velocity in terms of the gradient of the order parameter, Eq. (1.6). Although the condensate moves with the superfluid velocity, the superfluid density is not simply the density of the condensed atoms. In ^{4}He for example, the superfluid density approaches the total density as the temperature goes to zero, while only about 10 % of the particles are part of the condensate because of the strong interparticle interactions. The superfluid velocity is a property of a quantum mechanical state but in contrast to, e.g., the velocity of a single particle in a box, it is

not subject to large fluctuations since a macroscopic number of particles occupy this state. It can therefore be seen as an essentially classical variable which describes the quantum mechanical state the system finds itself in [12].

In order to introduce the superfluid velocity in a system, we use an approach developed by Leggett, which is based on the Hess-Fairbank effect and also provides a definition of superfluidity [14]. Equation (1.6) immediately leads to $\boldsymbol{\nabla} \times \boldsymbol{v}_s = 0$ and the application of Stokes theorem shows that the integral of $\boldsymbol{v}_s$ around a closed loop is zero

$$\oint_{\partial S} \boldsymbol{v}_s \cdot d\boldsymbol{l} = \int_S \boldsymbol{\nabla} \times \boldsymbol{v}_s \cdot d\boldsymbol{S} = 0. \tag{1.7}$$

On a nodal line, a region infinite in one dimension on which $|\Psi(\boldsymbol{r})| = 0$, the phase ϕ is not defined and therefore Stokes theorem can not be applied for paths ∂S which encircle a nodal line. However, it still holds that the phase ϕ is single valued modulo 2π. This leads to the Onsager-Feynman quantization condition

$$\oint \boldsymbol{v}_s \cdot d\boldsymbol{l} = \frac{1}{m} \oint \boldsymbol{\nabla}\phi \cdot d\boldsymbol{l} = n\frac{2\pi}{m}. \tag{1.8}$$

Consider a torus with major radius R and minor diameter d (Fig. 1.1) with $d/R \to 0$,

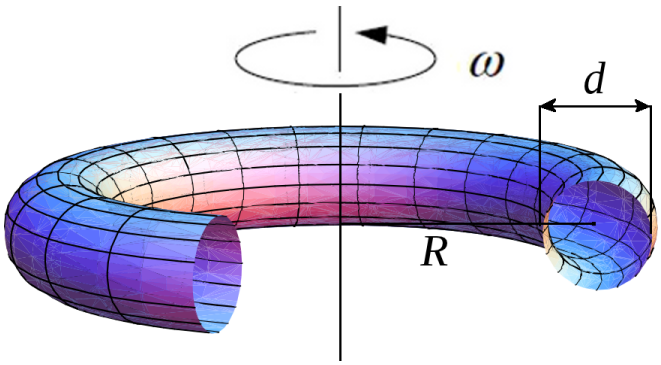

Figure 1.1: Image of a torus which provides the container for the superfluid in the Hess-Fairbank effect.

which acts as the container of the superfluid. When the torus is rotated with angular velocity ω, in equilibrium, the classical fluid angular velocity will simply be ω but a superfluid has to obey the above quantization condition

$$\begin{aligned} n\frac{2\pi}{m} = \oint \boldsymbol{v}_s \cdot d\boldsymbol{l} = R\int_0^{2\pi} v_{s,\theta} \cdot d\theta = 2\pi R \cdot v_{s,\theta} = 2\pi R^2 \cdot \omega_s, \\ \Rightarrow \omega_s = n\frac{1}{mR^2} = n \cdot \omega_c. \end{aligned} \tag{1.9}$$

It can be shown, that the equilibrium angular velocity is given by the value for n which is closest to ω/ω_c [14]. Rotating the torus with a small angular velocity $\omega < \omega_c/2$ thus leads to a rotation of the normal mass density, while the superfluid part stays at rest.

In the frame of reference co-rotating with the torus, only the superfluid mass density is in motion with velocity ωR. When staying in the frame of reference in which the torus is at rest, introducing a finite ω therefore leads to a finite velocity only in the superfluid part. The resulting change in the free energy can be interpreted as the kinetic energy of the superfluid mass density (neglecting a centrifugal term)

$$\Delta F = \frac{1}{2}\mathcal{V}\rho_s(\omega R)^2, \tag{1.10}$$

where $\mathcal{V}$ denotes the system volume. Thus the superfluid density can be obtained by calculating the difference in energy between the system at rest in the reference frame at rest (the lab frame) and the rotating system in the rotating frame of reference. In the rotating frame, the system is governed by the time independent Hamiltonian [12]

$$H_{\text{rot}} = H_0 - \boldsymbol{\omega}\cdot\boldsymbol{L}, \tag{1.11}$$

where H_0 is the many-body Hamiltonian for the system at rest and $\boldsymbol{L}$ denotes the total angular momentum. Note that even though H_{rot} describes the system in the rotating frame, it is expressed through the coordinates of the lab frame. The above Hamiltonian can be brought back to H_0 by a gauge transformation [15]

$$\begin{aligned} H_{\text{rot}} &\to H_0, \\ \psi_N &\to e^{-im\omega R^2\sum_i\theta_i}\psi_N. \end{aligned} \tag{1.12}$$

Here ψ_N denotes the N particle wavefunction which fulfills the single valued boundary conditions

$$\psi_N(\theta_1,...,\theta_i+2\pi,...,\theta_N) = \psi_N(\{\theta_i\}), \tag{1.13}$$

where θ_i is the angular coordinate of the ith particle. The above gauge transformation changes the boundary conditions, such that the wave function picks up a phase when taking one particle around the torus. The problem of finding the groundstate energy of H_{rot} therefore reduces to finding the groundstate energy of H_0 subject to twisted boundary conditions

$$\psi_N(\theta_1,...,\theta_i+2\pi,...,\theta_N) = e^{-i2\pi m\omega R^2}\psi_N(\{\theta_i\}). \tag{1.14}$$

In Eq. (1.12) we have again neglected a centrifugal term, such that the change in free energy is exactly given by Eq. (1.10). Thus changing the boundary conditions from single valued to twisted leads to a change in the free energy which can be interpreted as the kinetic energy of the superfluid part.

Using the following substitutions, we can generalize the above approach to an arbitrary geometry

$$\begin{aligned} 2\pi R &\to L, \\ \omega R &\to v_s, \\ \Delta\varphi = 2\pi m\omega R^2 &\to m v_s L, \end{aligned} \tag{1.15}$$

Changing the boundary conditions from single valued ($\Delta\varphi = 0$) to twisted

$$\psi_N(\boldsymbol{r}_1, ..., \boldsymbol{r}_i + L\hat{\boldsymbol{u}}, ..., \boldsymbol{r}_N) = e^{-i\Delta\varphi}\psi_N(\{\boldsymbol{r}_i\}), \tag{1.16}$$

where $\hat{\boldsymbol{u}}$ denotes the direction of the superfluid velocity, leads to a change in the free energy

$$\Delta F = \frac{1}{2}\mathcal{V}\rho_s\left(\frac{\Delta\varphi}{mL}\right)^2 = \frac{1}{2}\mathcal{V}\rho_s v_s^2. \tag{1.17}$$

To calculate the superfluid density, one therefore has to calculate the change in the free energy upon twisting the boundary conditions and compare it to the last expression. Per definition, a system shows superfluidity if the change in the free energy, and therefore the superfluid density, is finite.

The connection between the above approach of introducing a superfluid velocity and a similar method which uses a twist in the boundary conditions of the order parameter [16] remains an open question to us and is discussed in Appendix E.

1.2.2 The two-component superfluid

Since superfluid drag occurs in two-component superfluids, we have to generalize the concepts from the last subsection to the two-component case. Such a mixture was first discussed by Andreev and Bashkin in the context of ^{3}He-^{4}He [3]. In analogy to the two-fluid model, they describe the system using three-fluid hydrodynamics including two non-dissipative superflows $\boldsymbol{v}_{sA}$, $\boldsymbol{v}_{sB}$ and one normal flow $\boldsymbol{v}_n$. The superfluid drag is the effect, that the superflow of one component takes part in the mass-density current $\boldsymbol{j}$ of the other component

$$\begin{aligned} \boldsymbol{j}_\alpha &= \rho_{n\alpha}\boldsymbol{v}_n + \rho_{s\alpha}\boldsymbol{v}_{s\alpha} + \rho_d\boldsymbol{v}_{s\bar{\alpha}}, \\ \rho_\alpha &= \rho_{n\alpha} + \rho_{s\alpha} + \rho_d, \end{aligned} \tag{1.18}$$

where $\alpha \in (A, B)$ denotes one component, $\bar{\alpha}$ the other one, and ρ_α is the total mass density of component α. The coefficients in the mass-density current are the normal mass density, the superfluid density and the superfluid-drag coefficient respectively. For a finite ρ_d, the mass current densities of both components are finite, even in the situation where only one of the superflows is non-vanishing. In order to obtain a kinetic energy that is positive definite, the superfluid-drag coefficient has to fulfill the condition

$$\rho_d^2 < \rho_{sA}\rho_{sB}, \tag{1.19}$$

but it can in principle take either positive or negative values. Physically, the superfluid drag can be envisioned as follows. As a result of the interspecies interaction, the particles of one component are dressed by particles of the other component and drag them along in a non-dissipative fashion. The free energy of such a two-component superfluid can be expanded in the velocities and, for small velocities, it reads [3]

$$F = F_0 + \frac{1}{2}\mathcal{V}\left[\rho_n v_n^2 + \rho_{sA}v_{sA}^2 + \rho_{sB}v_{sB}^2 + 2\rho_d\boldsymbol{v}_{sA}\boldsymbol{v}_{sB}\right], \tag{1.20}$$

with F_0 being the part of the free energy that does not depend on the velocities and $\rho_n = \rho_{nA}+\rho_{nB}$. The superfluid drag therefore couples the two superflows of the system.

A question of experimental relevance is: what happens when we fix one of the superfluid velocities but let the system come to equilibrium in terms of the other one? The answer can be found by minimizing the free energy with respect to $\boldsymbol{v}_{sB}$ while keeping $\boldsymbol{v}_{sA}$ fixed

$$\begin{aligned}\left(\frac{\partial F}{\partial \boldsymbol{v}_{sB}}\right)_{\boldsymbol{v}_{sA}} &= \rho_{sB}\boldsymbol{v}_{sB} + \rho_d \boldsymbol{v}_{sA} = 0,\\ \Rightarrow \boldsymbol{v}_{sB} &= -\frac{\rho_d}{\rho_{sB}}\boldsymbol{v}_{sA}.\end{aligned} \tag{1.21}$$

The term in the free energy corresponding to the superfluid drag induces a superflow of component B in the direction opposite to the one of component A. For $\boldsymbol{v}_n = 0$, this leads to the mass-density currents

$$\begin{aligned}\boldsymbol{j}_A &= \left(\rho_{sA} - \frac{\rho_d^2}{\rho_{sB}}\right)\boldsymbol{v}_{sA},\\ \boldsymbol{j}_B &= 0.\end{aligned} \tag{1.22}$$

If we fix $\boldsymbol{v}_{sA}$, the moving A-particles will drag along particles of component B but at the same time, a superflow in B in the direction opposite of $\boldsymbol{v}_{sA}$ will be induced such that the total mass-density current of component B is zero. However, the B-superflow also drags along particles of component A leading to a "second order" reduction of its mass-density current.

We now generalize Leggetts approach of twisting the boundary conditions to the two-component case. Since the system supports two superflows, the phase twist depends on the particle component. Changing the boundary conditions from single valued ($\Delta\varphi_\alpha = 0$) to twisted

$$\psi_N(\boldsymbol{r}_{\alpha 1}, ..., \boldsymbol{r}_{\alpha i} + L\hat{\boldsymbol{u}}_\alpha, ..., \boldsymbol{r}_{\alpha N_\alpha}, \{\boldsymbol{r}_{\bar{\alpha} j}\}) = e^{-i\Delta\varphi_\alpha}\psi_N(\{\boldsymbol{r}_{\alpha i}, \boldsymbol{r}_{\bar{\alpha} j}\}), \tag{1.23}$$

where $\hat{\boldsymbol{u}}_\alpha$ denotes the direction of the superflow of component α, leads to a change in the free energy

$$\Delta F = \frac{1}{2}\mathcal{V}\left[\rho_{sA}v_{sA}^2 + \rho_{sB}v_{sB}^2 + 2\rho_d \boldsymbol{v}_{sA}\boldsymbol{v}_{sB}\right]. \tag{1.24}$$

The superfluid velocities are given by the relation

$$\boldsymbol{v}_{s\alpha} = \frac{\Delta\varphi_\alpha}{m_\alpha L}\hat{\boldsymbol{u}}_\alpha. \tag{1.25}$$

1.3 Ultracold atoms

The term ultracold atoms usually implies ultracold alkali atoms, since they can be readily produced and manipulated experimentally. An atomic beam with a relatively high density can be generated by heating an alkali metal in an oven with a small

opening. Their strong cyclic transition from the ground state to the excited state, the $ns \to np$ transition of the single valence electron, allows for manipulation of the atoms by laser light in the visible spectrum, where enough laser power is available [17]. The alkalis have an odd number of electrons, thus all the isotopes with an odd mass number are comprised of an even number of fermions and are therefore bosonic, e.g. ^{133}Cs, ^{87}Rb, ^{85}Rb, ^{41}K, ^{23}Na, and ^{7}Li.

Since the successes of laser- and evaporative-cooling techniques, there has been tremendous progress in the study of interactions in the ultracold regime both in experiment and in theory. From a theoretical point of view, justified approximations in Bose-condensed alkali atoms significantly simplify their description. The two-body potential for states with finite angular momentum contains a centrifugal energy barrier which is around 1 mK. At ultracold temperatures, scattering in finite angular momentum states is therefore frozen out and only s-wave scattering is of importance [18]. Scattering is thus determined by the s-wave scattering length a_s, which is positive for repulsive and negative for attractive interactions. For repulsive interactions, it can be visualized as the radius of a hard-sphere potential which would lead to the same scattering wavefunction. Since a_s is usually much smaller than all the other length scales in the system (thermal de Broglie wavelength, interparticle spacing, and zero-point length of the trap), the gas parameter na_s^3 (n is the density) is much smaller than one and the strong but short-ranged interactions only rarely lead to scattering events. In order to avoid the calculation of the complicated short-range correlations, it is convenient to integrate out the finite-momentum degrees of freedom which leads to an effective contact interaction [19]

$$U(\boldsymbol{r} - \boldsymbol{r}') = \gamma\delta(\boldsymbol{r} - \boldsymbol{r}'), \quad \text{with} \quad \gamma = \frac{2\pi}{m}a_s, \tag{1.26}$$

where m is the reduced mass.

Since the value of a_s depends very sensitively on the involved hyperfine states and external fields, it can in general not be predicted accurately but has to be measured [20]. Its field dependence can however be used to tune the scattering length via Feshbach resonance by varying an external parameter such as the magnetic field. A Feshbach resonance occurs if there is a bound state (with energy E_{res}), provided by a potential which corresponds to a different set of quantum numbers (channel), close to the energy of the approaching particles (E_0) as illustrated in Fig. 1.2. Because of energy conservation, the two particles together need to have the same energy before and after the scattering event and can therefore only leave through the same channel as they enter (the open channel). They can however virtually scatter in and out of a bound state provided by a closed channel. This leads to second order corrections in their potential energy when they are close to each other. These corrections are negative when $E_{\text{res}} > E_0$ which leads to an effective attraction and thus a negative scattering length. If $E_{\text{res}} < E$, second order perturbation gives a positive energy shift, leading to an effective repulsion. Around such a resonance, the scattering length is therefore of the form

$$a_s \propto \frac{1}{E - E_{\text{res}}}. \tag{1.27}$$

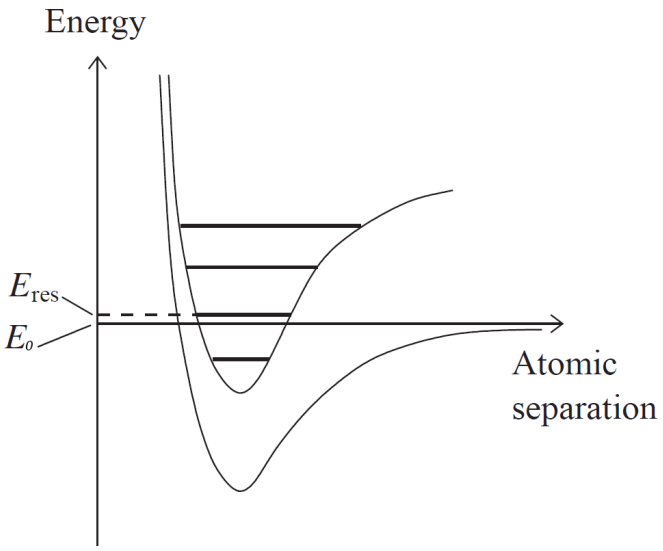

Figure 1.2: Taken from [19]. Two potentials corresponding to two different channels. The energy of the approaching atoms in the open channel is shifted by nearby bound states in the closed channel.

By applying an external field, one can tune $E - E_{\text{res}}$ and therefore also the scattering length. Since a_s diverges at resonance, one can in principle sweep it from $-\infty$ to ∞, switching the interactions from attractive to repulsive. However, If the magnitude of a_s becomes too large, rapid three-body processes destroy the atom gas [1].

1.4 Optical lattices

Two different types of forces act on an atom in a light field, the scattering force and the dipole force. The dissipative scattering force is based on absorption and subsequent spontaneous emission of photons and can be used to cool atoms. The dipole force on the other hand is a conservative force, based on stimulated emission and can be used to trap atoms and to create optical lattices [17]. It has its origin in the interaction between the induced dipole moment of the atom and the electric field of the light. Since the dipole force is conservative, it can be written as the gradient of a potential V_{dip}, which is termed optical lattice because it is proportional to the light field intensity

$$V_{\text{dip}} = -\frac{1}{2}\alpha\langle E(\boldsymbol{r},t)^2\rangle_t \,, \tag{1.28}$$

where α is the real part of the polarizability, which depends on the frequency of the light, E is the electric field, and $\langle ...\rangle_t$ denotes the time average. The resulting shift in the atomic energy levels is known as the AC-Stark shift. Close to an atomic resonance, the polarizability is positive for frequencies below resonance (red detuning) and negative for frequencies above resonance (blue detuning). The atoms therefore accumulate in

the intensity maxima for red detuning, while for blue detuning they are attracted by the intensity minima of the light field [19].

In this work, we have investigated the superfluid drag in three different two-dimensional lattice potentials which are shown in Fig. 1.3. One of them is the well known lattice of square geometry created by counterpropagating laser beams of equal wavelength and intensity in all dimensions [cf. Fig. 1.3 (c)], here denoted four-beam square lattice (4BSL). Adding up the electric fields of the laser beams and averaging over time leads to the potential (omitting an unimportant constant term)

$$V^{\mathrm{4B}}(\boldsymbol{r}) = \frac{V_0}{2}\Big[\cos(2k_L x) + \cos(2k_L y)\Big], \tag{1.29}$$

here $k_L = 2\pi/\lambda_L$ is the wave vector of the lasers and $V_0 = -\alpha I_0/2\epsilon_0 c$ is the light-shift strength parameter with the light field intensity I_0, the speed of light c and the vacuum permittivity ϵ_0. Since this potential is separable [it can be written as $V(\boldsymbol{r}) = V_x(x) + V_y(y)$], the eigenfunction of its single particle Hamiltonian can be written as a product $\psi(\boldsymbol{r}) = \psi_x(x)\psi_y(y)$, turning the single-particle eigenvalue equation into a one-dimensional problem. In addition to its mathematical simplicity, this optical lattice is also the least demanding one in terms of experimental realization.

To investigate the influence of the lattice geometry on the superfluid drag, we investigated two additional optical lattices which are created by three in-plane laser beams of equal wavelength and intensity. The three-beam lattice of triangular geometry [3BTL, Fig. 1.3 (a)] and of square geometry [3BSL, Fig. 1.3 (b)]. These three-beam lattices are thoroughly discussed in Ref. 8. The wave vectors which are needed to create the lattices can be parametrized as

$$\boldsymbol{k}_i \equiv k_L \begin{pmatrix} \cos\theta_i \\ \sin\theta_i \end{pmatrix} \qquad (i = 1, 2, 3), \tag{1.30}$$

their reciprocal-lattice basis vectors are given by the relation

$$\boldsymbol{b}_i \equiv \boldsymbol{k}_i - \boldsymbol{k}_{i+1} \qquad (i = 1, 2), \tag{1.31}$$

and the resulting optical-lattice potential reads (again omitting a constant)

$$V^{\mathrm{3B}}(\boldsymbol{r}) = \frac{V_0}{2}\Big[\cos(\boldsymbol{b}_1 \cdot \boldsymbol{r}) + \cos(\boldsymbol{b}_2 \cdot \boldsymbol{r}) + \cos([\boldsymbol{b}_1 + \boldsymbol{b}_2] \cdot \boldsymbol{r})\Big]. \tag{1.32}$$

The explicit wave vectors and lattice vectors of the 3BTL and 3BSL are given in Appendix A.

When filling an optical lattice with two different species, e.g. two different atomic species or two hyperfine states, in general the potential does not have the same form for the two because the light-shift strength parameter depends on the polarizability of the individual state. By modifying the laser polarizations, it is therefore possible to create lattices which strongly depend on the internal states involved. This allows for state selectively moving the lattice [2] or the formation of antiferromagnetic ordering [21]. In this work, however, we only consider systems where the lattice potential is approximately equal for both species. This is not an unreasonable assumption since such systems are experimentally accessible [22].

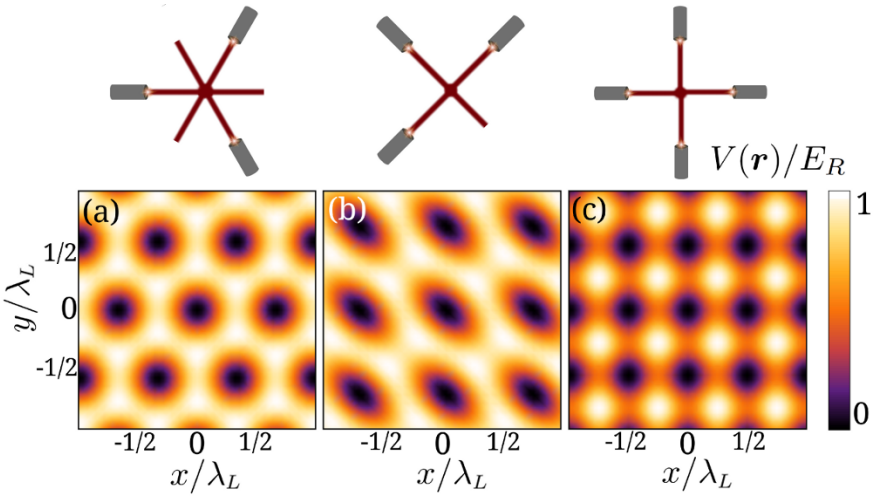

Figure 1.3: Laser configurations and the resulting optical-lattice potentials, with their minima set equal to zero, in units of the recoil energy $E_R = k_L^2/2m$, the kinetic energy an atom receives upon absorbing a photon from the lattice. (a) 3BTL, (b) 3BSL, (c) 4BSL. For these plots $V_0 = -E_R/2$.

1.5 The Bose-Hubbard model

In this chapter, we sketch the derivation of the Bose-Hubbard Hamiltonian, which is used to describe a system of ultracold atoms in an optical lattice [23]. Using the effective contact interaction, Eq. (1.26), the Hamiltonian of a system of two different kinds of bosons in an optical-lattice potential $V(\boldsymbol{r})$ may be written as:

$$\begin{aligned} H = &\sum_{\alpha} \int d\boldsymbol{r}\, \psi_\alpha^\dagger(\boldsymbol{r}) \left[-\frac{\nabla^2}{2m_\alpha} - \mu_\alpha + V(\boldsymbol{r}) \right] \psi_\alpha(\boldsymbol{r}) \\ &+ \frac{1}{2} \sum_{\alpha\beta} \gamma_{\alpha\beta} \int d\boldsymbol{r}\, \psi_\alpha^\dagger(\boldsymbol{r}) \psi_\beta^\dagger(\boldsymbol{r}) \psi_\beta(\boldsymbol{r}) \psi_\alpha(\boldsymbol{r}). \end{aligned} \tag{1.33}$$

with $\alpha, \beta \in (A, B)$ denoting boson components, μ_α the chemical potential and $V(\boldsymbol{r})$ the optical lattice potential. The interaction parameters (in three dimensions) are given by:

$$\gamma_{\alpha\beta} = \begin{cases} 4\pi a_\alpha/m_\alpha, & \text{if } \alpha = \beta, \\ 2\pi(m_A + m_B)a_{AB}/(m_A m_B), & \text{if } \alpha \neq \beta, \end{cases} \tag{1.34}$$

where the parameters a_α, a_{AB} are the respective intra- and interspecies s-wave scattering lengths. Here we neglect a slowly varying trapping potential, which in practice has to be used to confine the particles, such that they do not escape the region of the optical lattice. Furthermore, we assume that all particles are in the lowest band. This is a good description of the system if $k_B T \ll E_{\text{gap}}$ and $nU_{\alpha\beta} \ll E_{\text{gap}}$ [8], where E_{gap} is the energy gap to the first excited band, n is the average site occupation and $U_{\alpha\beta}$ is the on site interaction which will be defined later [cf. Eq. (1.39)]. At $T = 0$, our numerical

calculations show that these conditions are fulfilled at least to a lattice depth as shallow as one recoil energy for the 3BLs.

We expand the boson field operators in the Wannier functions of the lowest band

$$\psi_\alpha(\boldsymbol{r}) = \sum_i b_{i\alpha} W_\alpha(\boldsymbol{r} - \boldsymbol{R}_i), \tag{1.35}$$

where $\boldsymbol{R}_i$ is the lattice vector of site i. This leads to the Hamiltonian

$$H = -\sum_{ij,\alpha} J_{ij\alpha} b^\dagger_{i\alpha} b_{j\alpha} + \frac{1}{2} \sum_{\substack{ijkl \\ \alpha\beta}} U_{ijkl\alpha\beta} b^\dagger_{i\alpha} b^\dagger_{j\beta} b_{k\beta} b_{l\alpha} \,, \tag{1.36}$$

with the parameters

$$\begin{aligned} J_{ij\alpha} &= -\int d\boldsymbol{r}\, W^*_\alpha(\boldsymbol{r} - \boldsymbol{R}_i) \left[-\frac{\nabla^2}{2m_\alpha} - \mu_\alpha + V(\boldsymbol{r}) \right] W_\alpha(\boldsymbol{r} - \boldsymbol{R}_j), \\ U_{ijkl\alpha\beta} &= \gamma_{\alpha\beta} \int d\boldsymbol{r}\, W^*_\alpha(\boldsymbol{r} - \boldsymbol{R}_i) W^*_\beta(\boldsymbol{r} - \boldsymbol{R}_j) W_\beta(\boldsymbol{r} - \boldsymbol{R}_k) W_\alpha(\boldsymbol{r} - \boldsymbol{R}_l). \end{aligned} \tag{1.37}$$

Here the diagonal and off-diagonal elements of $J_{ij\alpha}$ correspond to the on-site energies and the tunneling amplitudes respectively.

Note that experimentally, only quasi two-dimensional systems can be created in our three-dimensional world. To describe such a system, the above expressions should therefore be evaluated with three-dimensional quantities and some care has to be taken when reducing the system to quasi two-dimensionality (cf. Sec. 3.2).

Numerically, we find that the overlap of the Wannier functions at different lattice sites is sufficiently small to neglect all inter-site interactions (they are about two orders of magnitude smaller than on-site interactions). This approximation, together with the discrete translational invariance of the system (note that this implies $J_{ij\alpha} = J_{ji\alpha} \in \mathbb{R}$) leads to the Bose-Hubbard Hamiltonian

$$H = -\sum_{ij,\alpha} J_{ij\alpha} b^\dagger_{i\alpha} b_{j\alpha} + \frac{1}{2} \sum_{i,\alpha\beta} U_{\alpha\beta} b^\dagger_{i\alpha} b^\dagger_{i\beta} b_{i\beta} b_{i\alpha} \,, \tag{1.38}$$

with interaction parameters that are no longer dependent on the lattice sites

$$U_{\alpha\beta} = \gamma_{\alpha\beta} \int d\boldsymbol{r}\ |W_\alpha(\boldsymbol{r})|^2 \left|W_\beta(\boldsymbol{r})\right|^2 . \tag{1.39}$$

In this work we only consider repulsive interactions, i.e. $U_{\alpha\beta} > 0$ for all α, β.

The above Hamiltonian describes particles on a lattice which gain kinetic energy by hopping from one lattice site to another and provide interaction energy when occupying the same site. Increasing the lattice depth confines the particles leading to an exponential decrease in the kinetic energy and an algebraic increase in the interaction energy (see Fig. 1.4). At a commensurate filling of the lattice, when the interaction becomes sufficiently large compared to the tunneling between sites, the system orders

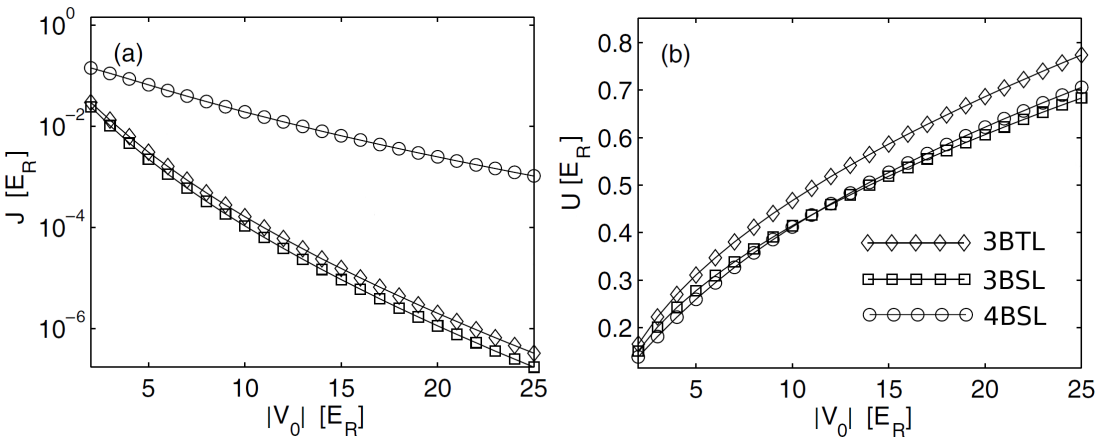

Figure 1.4: Taken from [8]. Bose-Hubbard parameters for the three-beam triangular lattice (3BTL), three-beam square lattice (3BSL) and the four-beam square lattice (4BSL). (a) J corresponds to the nearest neighbor hopping amplitude, (b) U to the interaction parameter of a single species residing in the lattice.

itself in a state where each site is occupied by the same integer number of particles and a SF-MI transition occurs. In experiments, the trapping potential leads to a local variation of the chemical potential which can lead to a local commensurate filling and several SF and MI phases can be observed at the same time as illustrated in Fig. 1.5.

1.6 Experimental status

Although systems in which superfluid drag occurs can be experimentally realized, it has so far not been measured. Especially for ultracold atoms this is not surprising since in such systems the superfluid density has not been measured either (although a proposal for such an experiment exists [25]) and the drag is an even less tangible quantity. Performing experiments on the superfluid drag requires the mixture of two superfluids. This can be achieved by Bose condensing two different atomic species or two internal hyperfine states of the same atomic species. Since in our work we neglect interconversion of the two components, the hyperfine states would need to be separated by an energy barrier which they can not overcome. To achieve a stable mixture, the interactions have to fulfill the following condition

$$U_{AB}^2 < U_A U_B, \tag{1.40}$$

or else the interspecies interaction becomes too strong compared to the intraspecies interactions and phase separation occurs. In the case of two different atomic species this poses a problem since the above relation is usually not fulfilled [26, 27]. Using Feshbach resonances, it is possible to tune the s-wave scattering length to values where the two species mix. By this method, tunable miscibility has been achieved for ^{85}Rb-^{87}Rb by the Wieman group [28] and for ^{41}K-^{87}Rb by the Inguscio group [29]. In an optical lattice however, only a phase separated mixture of ^{41}K-^{87}Rb has so far been realized [22].

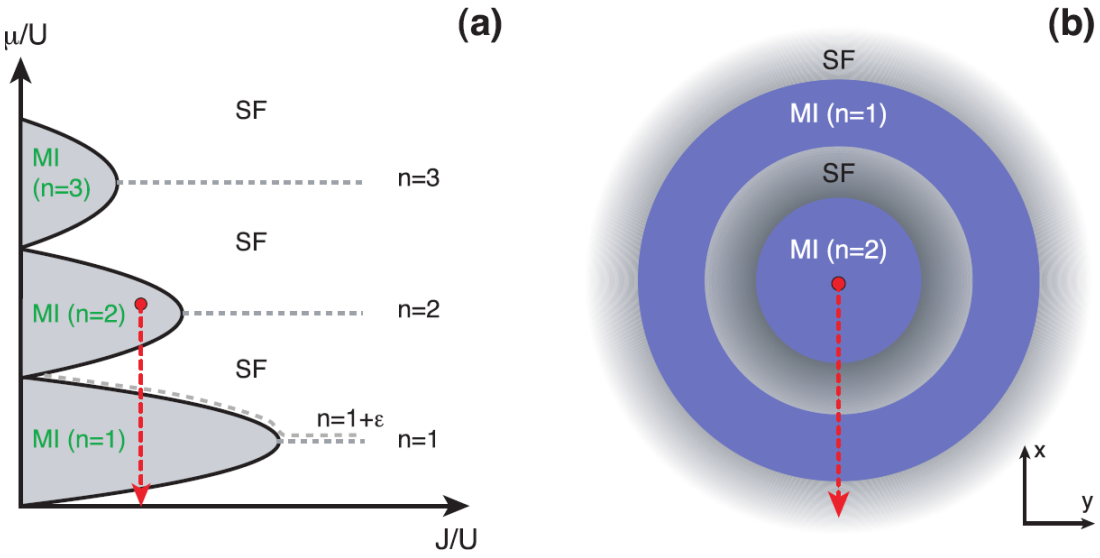

Figure 1.5: Taken from [24]. (a) Phase diagram for the Bose-Hubbard model, n denotes the number of particles per site. (b) in a trapping potential, the chemical potential varies in space leading to different, spacially separated phases. The red arrow illustrates how the chemical potential decreases away from the trap center.

In the case of two different hyperfine states of ^{87}Rb, phase separation seems to be less of a problem. The first mixture of two internal hyperfine states was therefore already realized in 1997 [30] and by now these mixtures have been observed not only in cubic [31] but also in spin dependent hexagonal optical lattices [21].

Chapter 2

Derivation of the superfluid-drag coefficient

In this chapter, we present a derivation of an expression for the superfluid-drag coefficient in an arbitrary lattice, analogous to Ref. 5 where this has been done for a cubic lattice. This expression is written in dependence of the band dispersion, its derivative and the Hubbard-interaction parameters, which will be calculated numerically. We use a numerical approach, in contrast to tight binding, mainly because it should not be taken for granted that tight binding leads to reliable results in the limit of a weak optical lattice, which ensures the superfluid phase.

To switch from the real-space lattice description to momentum space, we use the Fourier-transformed boson operators

$$b_{i\alpha} = \frac{1}{\sqrt{N}} \sum_{\boldsymbol{k}} b_{\boldsymbol{k}\alpha} e^{-i\boldsymbol{k}\boldsymbol{r}_i}, \tag{2.1}$$

where N is the number of lattice sites. Inserting this relation into Eq. (1.38) leads to (the calculation is given in Appendix B.1)

$$H = \sum_{\boldsymbol{k},\alpha} \varepsilon_{\boldsymbol{k}\alpha} b^\dagger_{\boldsymbol{k}\alpha} b_{\boldsymbol{k}\alpha} + \frac{1}{2N} \sum_{\alpha\beta} U_{\alpha\beta} \sum_{\boldsymbol{k}_1 \ldots \boldsymbol{k}_4} b^\dagger_{\boldsymbol{k}_1\alpha} b^\dagger_{\boldsymbol{k}_2\beta} b_{\boldsymbol{k}_3\beta} b_{\boldsymbol{k}_4\alpha} \delta_{\boldsymbol{k}_1+\boldsymbol{k}_2,\boldsymbol{k}_3+\boldsymbol{k}_4}. \tag{2.2}$$

The parameter $\varepsilon_{\boldsymbol{k}\alpha}$ is the aforementioned band dispersion and $U_{\alpha\beta}$ are the Hubbard-interaction parameters which will be calculated numerically.

2.1 The Bogoliubov approximation

In order to diagonalize the Hamiltonian, we use the Bogoliubov approximation to replace the Hamiltonian with a bilinear operator. Considering the case where the $\boldsymbol{k} = 0$ state is macroscopically occupied, the corresponding boson creation and annihilation

operators commute to a very good approximation. Thus we can replace them by c-numbers [19]

$$\begin{aligned} \langle b_{0\alpha} b_{0\alpha}^\dagger \rangle = \langle b_{0\alpha}^\dagger b_{0\alpha} \rangle + 1 \approx \langle b_{0\alpha}^\dagger b_{0\alpha} \rangle = N_{0\alpha}, \\ b_{0\alpha} \approx b_{0\alpha}^\dagger \approx \sqrt{N_{0\alpha}}\,. \end{aligned} \tag{2.3}$$

Therefore, the interaction terms which involve more $\boldsymbol{k} = 0$ states dominate over the terms involving more $\boldsymbol{k} \neq 0$ states. This justifies neglecting all the terms which are of higher order then bilinear in the remaining creation-/annihilation operators. The resulting Hamiltonian reads

$$H = H_0 + {\sum_{\boldsymbol{k}}}' \left[H_{AB} + \sum_\alpha H_\alpha \right], \tag{2.4}$$

where the primed sum runs over all $\boldsymbol{k}$-states except $\boldsymbol{k} = 0$. The different terms are explicitly given by

$$\begin{aligned} H_0 &= \sum_\alpha \left[\varepsilon_{0\alpha} N_\alpha + \frac{N_\alpha^2}{2N} U_\alpha \right] + \frac{N_A N_B}{N} U_{AB}\,, \\ H_\alpha &= \underbrace{(\varepsilon_{\boldsymbol{k}\alpha} - \varepsilon_{0\alpha} + n_\alpha U_\alpha)}_{E_{\boldsymbol{k}}^\alpha} b_{\boldsymbol{k}\alpha}^\dagger b_{\boldsymbol{k}\alpha} + \frac{n_\alpha}{2} U_\alpha \left(b_{\boldsymbol{k}\alpha} b_{-\boldsymbol{k}\alpha} + b_{\boldsymbol{k}\alpha}^\dagger b_{-\boldsymbol{k}\alpha}^\dagger \right), \\ H_{AB} &= \sqrt{n_A n_B}\, U_{AB} \left(b_{\boldsymbol{k}A}^\dagger b_{\boldsymbol{k}B} + b_{\boldsymbol{k}B}^\dagger b_{\boldsymbol{k}A} + b_{\boldsymbol{k}A} b_{-\boldsymbol{k}B} + b_{\boldsymbol{k}A}^\dagger b_{-\boldsymbol{k}B}^\dagger \right). \end{aligned} \tag{2.5}$$

Here $n_\alpha \equiv N_\alpha / N$ is the particle density of component α and for simplicity we omit double indices, $U_\alpha \equiv U_{\alpha\alpha}$. The derivation of Eq. (2.4) can be found in Appendix B.2.

Since the Bogoliubov approximation relies on the macroscopic occupation of the ground state, it is not suitable to describe a large depletion of the condensate and therefore only holds in the SF phase for weakly interacting bosons.

2.2 Matrix notation and diagonalization

The problem of diagonalizing a bilinear Hamiltonian of an assembly of bosons using the following matrix notation is discussed in more detail in Ref. 32. Upon defining the column vector

$$|b_{\boldsymbol{k}}\rangle \equiv \left(b_{\boldsymbol{k}A},\, b_{\boldsymbol{k}B},\, b_{-\boldsymbol{k}A}^\dagger,\, b_{-\boldsymbol{k}B}^\dagger \right), \tag{2.6}$$

and the respective row vector

$$\langle b_{\boldsymbol{k}}| \equiv |b_{\boldsymbol{k}}\rangle^\dagger = \left(b_{\boldsymbol{k}A}^\dagger \;\; b_{\boldsymbol{k}B}^\dagger \;\; b_{-\boldsymbol{k}A} \;\; b_{-\boldsymbol{k}B} \right), \tag{2.7}$$

the Hamiltonian in Eq. (2.4) can be written in a compact matrix notation:

$$H = H_0 - \frac{1}{2} {\sum_{\boldsymbol{k},\alpha}}' E_{\boldsymbol{k}}^\alpha + \frac{1}{2} {\sum_{\boldsymbol{k}}}' \langle b_{\boldsymbol{k}}|\, \mathcal{M}_{\boldsymbol{k}}\, |b_{\boldsymbol{k}}\rangle\,. \tag{2.8}$$

Here we introduced

$$\mathcal{M}_{\boldsymbol{k}} = \begin{pmatrix} E^A_{\boldsymbol{k}} & F_{AB} & F_A & F_{AB} \\ F_{AB} & E^B_{\boldsymbol{k}} & F_{AB} & F_B \\ F_A & F_{AB} & E^A_{-\boldsymbol{k}} & F_{AB} \\ F_{AB} & F_B & F_{AB} & E^B_{-\boldsymbol{k}} \end{pmatrix}, \tag{2.9}$$

where $F_\alpha = n_\alpha U_\alpha$, $F_{AB} = \sqrt{n_A n_B}\, U_{AB}$, $E^\alpha_{\boldsymbol{k}} = \epsilon^\alpha_{\boldsymbol{k}} + F_\alpha$ and $\epsilon^\alpha_{\boldsymbol{k}} = \varepsilon_{\boldsymbol{k}\alpha} - \varepsilon_{0\alpha}$.

Note that $\epsilon^\alpha_{\boldsymbol{k}}$, and therefore also $E^\alpha_{\boldsymbol{k}}$, are by construction invariant under the transformation $\boldsymbol{k} \to -\boldsymbol{k}$ [cf. (B.4)]. Diagonalization of the Hamiltonian given by Eq. (2.8) is equivalent to expressing it in the form

$$H = H_0 - \frac{1}{2}{\sum_{\boldsymbol{k},\alpha}}' E^\alpha_{\boldsymbol{k}} + \frac{1}{2}{\sum_{\boldsymbol{k}}}' \langle \beta_{\boldsymbol{k}} | \, \mathcal{D}_{\boldsymbol{k}} \, | \beta_{\boldsymbol{k}} \rangle \,, \tag{2.10}$$

where the diagonal matrix $\mathcal{D}_{\boldsymbol{k}}$ contains the excitation energies. By demanding preservation of the bosonic commutation relations, it turns out that it is not the matrix $\mathcal{M}_{\boldsymbol{k}}$ which has to be diagonalized in order to retrieve $\mathcal{D}_{\boldsymbol{k}}$ as explained in the following.

In the vector representation of the creation/annihilation operators, the bosonic commutation relations can be expressed as

$$|b_{\boldsymbol{k}}\rangle \langle b_{\boldsymbol{k}}| - \left(|b^\dagger_{\boldsymbol{k}}\rangle \langle b^\dagger_{\boldsymbol{k}}|\right)^T = \sigma_3, \tag{2.11}$$

where the 4×4 matrix σ_3 is given by

$$\sigma_3 = \begin{pmatrix} \mathbb{1}_2 & 0_2 \\ 0_2 & -\mathbb{1}_2 \end{pmatrix}. \tag{2.12}$$

Note that $|b^\dagger_{\boldsymbol{k}}\rangle$ means taking the Hermitian conjugate of the elements of $|b_{\boldsymbol{k}}\rangle$, it is therefore still a column vector and not equal to $|b_{\boldsymbol{k}}\rangle^\dagger = \langle b_{\boldsymbol{k}}|$ but equal to $\langle b_{\boldsymbol{k}}|^T$.

We demand that the new basis $|\beta_{\boldsymbol{k}}\rangle$, which is related to the old one by a transformation matrix $|\beta_{\boldsymbol{k}}\rangle = T^\dagger_{\boldsymbol{k}} |b_{\boldsymbol{k}}\rangle$, also satisfies the bosonic commutation relations:

$$\begin{aligned} \sigma_3 &= |\beta_{\boldsymbol{k}}\rangle \langle \beta_{\boldsymbol{k}}| - \left(|\beta^\dagger_{\boldsymbol{k}}\rangle \langle \beta^\dagger_{\boldsymbol{k}}|\right)^T \\ &= T^\dagger_{\boldsymbol{k}} |b_{\boldsymbol{k}}\rangle \langle b_{\boldsymbol{k}}| T_{\boldsymbol{k}} - \left(T^T_{\boldsymbol{k}} |b^\dagger_{\boldsymbol{k}}\rangle \langle b^\dagger_{\boldsymbol{k}}| T^{\dagger T}_{\boldsymbol{k}}\right)^T \\ &= T^\dagger_{\boldsymbol{k}} \left[|b_{\boldsymbol{k}}\rangle \langle b_{\boldsymbol{k}}| - \left(|b^\dagger_{\boldsymbol{k}}\rangle \langle b^\dagger_{\boldsymbol{k}}|\right)^T \right] T_{\boldsymbol{k}} = T^\dagger_{\boldsymbol{k}} \sigma_3 T_{\boldsymbol{k}} \\ &\Rightarrow T^{-1}_{\boldsymbol{k}} = \sigma_3 T^\dagger_{\boldsymbol{k}} \sigma_3. \end{aligned} \tag{2.13}$$

Here we used $|\beta^\dagger_{\boldsymbol{k}}\rangle = T^T_{\boldsymbol{k}} |b^\dagger_{\boldsymbol{k}}\rangle$ which follows from $|b^\dagger_{\boldsymbol{k}}\rangle = \langle b_{\boldsymbol{k}}|^T$. Eqs. (2.8, 2.10) imply the relation

$$T_{\boldsymbol{k}} \mathcal{D}_{\boldsymbol{k}} T^\dagger_{\boldsymbol{k}} = \mathcal{M}_{\boldsymbol{k}}, \tag{2.14}$$

from which one obtains, using Eq. (2.13),

$$\begin{aligned} &T_{\boldsymbol{k}} \left(\mathcal{D}_{\boldsymbol{k}} \sigma_3\right) T^{-1}_{\boldsymbol{k}} = T_{\boldsymbol{k}} \mathcal{D}_{\boldsymbol{k}} T^\dagger_{\boldsymbol{k}} \sigma_3 = \mathcal{M}_{\boldsymbol{k}} \sigma_3 \\ &\Rightarrow T^{-1}_{\boldsymbol{k}} \left(\mathcal{M}_{\boldsymbol{k}} \sigma_3\right) T_{\boldsymbol{k}} = \mathcal{D}_{\boldsymbol{k}} \sigma_3. \end{aligned} \tag{2.15}$$

This means that the matrix $T_{\boldsymbol{k}}$ diagonalizes $\mathcal{M}_{\boldsymbol{k}}\sigma_3$. The resulting matrix $\mathcal{D}_{\boldsymbol{k}}\sigma_3$ contains the excitation spectrum with the two lower entries being negative because the matrix $\mathcal{D}_{\boldsymbol{k}}$ has only positive entries.

Evaluating the determinant $|\mathcal{M}_{\boldsymbol{k}}\sigma_3 - \mathcal{E}_{\boldsymbol{k}}\mathbb{1}_4| = 0$ yields four distinct eigenvalues $\mathcal{E}_{\boldsymbol{k}} = \pm\mathcal{E}_{\boldsymbol{k}\sigma}$, $\sigma = \pm 1$. As mentioned above, only the positive eigenvalues are of physical interest. When there are no superflows, they read

$$\begin{aligned}\mathcal{E}^0_{\boldsymbol{k}\sigma} = \frac{1}{\sqrt{2}}\Bigg\{&\epsilon^A_{\boldsymbol{k}}\left(\epsilon^A_{\boldsymbol{k}} + 2F_A\right) + \epsilon^B_{\boldsymbol{k}}\left(\epsilon^B_{\boldsymbol{k}} + 2F_B\right)\\ &+ \sigma\sqrt{\left[\epsilon^A_{\boldsymbol{k}}\left(\epsilon^A_{\boldsymbol{k}} + 2F_A\right) - \epsilon^B_{\boldsymbol{k}}\left(\epsilon^B_{\boldsymbol{k}} + 2F_B\right)\right]^2 + 16F^2_{AB}\epsilon^A_{\boldsymbol{k}}\epsilon^B_{\boldsymbol{k}}}\Bigg\}^{1/2}.\end{aligned} \tag{2.16}$$

Because $\epsilon^\alpha_{\boldsymbol{k}} = \varepsilon_{\boldsymbol{k}\alpha} - \varepsilon_{0\alpha}$ one can easily see that this two-component spectrum has no gap, i.e. $\mathcal{E}_{\boldsymbol{k}\sigma} \to 0$ as $\boldsymbol{k} \to 0$. This implies that the Bogoliubov approximation can not describe the gapped Mott phase because it is restricted to a small depletion of the condensate. When the interspecies interaction become to strong, i.e. when the inequality (1.40) is no longer fulfilled, the above expression becomes imaginary and phase separation occurs.

By inserting the diagonalized matrix

$$\mathcal{D}_{\boldsymbol{k}} = \mathrm{diag}(\mathcal{E}_{\boldsymbol{k}+}, \mathcal{E}_{\boldsymbol{k}-}, \mathcal{E}_{-\boldsymbol{k}+}, \mathcal{E}_{-\boldsymbol{k}-}), \tag{2.17}$$

in Eq. (2.10) we obtain the Hamiltonian

$$H = H_0 - \frac{1}{2}{\sum_{\boldsymbol{k},\alpha}}' E^\alpha_{\boldsymbol{k}} + {\sum_{\boldsymbol{k},\sigma}}' \mathcal{E}_{\boldsymbol{k}\sigma}\left(\beta^\dagger_{\boldsymbol{k}\sigma}\beta_{\boldsymbol{k}\sigma} + \frac{1}{2}\right). \tag{2.18}$$

2.3 Superfluid velocity and superfluid drag

At zero temperature, the free energy is equal to the expectation value of the Hamiltonian and there are no quasiparticles excited, i.e., $\langle\beta^\dagger_{\boldsymbol{k}\sigma}\beta_{\boldsymbol{k}\sigma}\rangle = 0$. The free energy thus reads

$$F_{T=0} = \langle H_0\rangle + \frac{1}{2}{\sum_{\boldsymbol{k}}}'\left[\mathcal{E}_{\boldsymbol{k}+} + \mathcal{E}_{\boldsymbol{k}-} - E^A_{\boldsymbol{k}} - E^B_{\boldsymbol{k}}\right]. \tag{2.19}$$

To find the superfluid-drag coefficient ρ_d, we expand Eq. (2.19) in the superfluid velocities and compare it to the free energy of a two-component superfluid with small superfluid velocities, Eq. (1.20).

As discussed in Sec. 1.2.2, introducing superfluid velocities can be achieved by twisting the boundary conditions, which means that the many-body wavefunction picks up a phase when a particle is taken from one side of the (periodic) system to the other. Due to the discrete translational symmetry of the system, the phase accumulated by taking a particle from one lattice point to the next always has to be same. The twist in the boundary conditions can therefore be achieved by the transformation

$$b^\dagger_{j\alpha}b_{i\alpha} \to e^{-i\frac{\Delta\varphi_\alpha}{L}\hat{\boldsymbol{u}}_\alpha(\boldsymbol{r}_j - \boldsymbol{r}_i)}b^\dagger_{j\alpha}b_{i\alpha}. \tag{2.20}$$

The accumulated phase, when taking a particle from site i to site j, corresponds to the phase shift per length, multiplied with the separation of the two sites in the direction of the superflow. On the single particle operators, this transformation has the effect

$$\begin{aligned} b_{i\alpha} \to e^{i\frac{\Delta\varphi_\alpha}{L}\hat{\boldsymbol{u}}_\alpha \boldsymbol{r}_i} b_{i\alpha} &= e^{im_\alpha \boldsymbol{v}_{s\alpha}\boldsymbol{r}_i} b_{i\alpha} \\ &= \frac{1}{\sqrt{N}} \sum_{\boldsymbol{k}} b_{\boldsymbol{k}\alpha} e^{-i(\boldsymbol{k}-m_\alpha \boldsymbol{v}_{s\alpha})\boldsymbol{r}_i}, \end{aligned} \tag{2.21}$$

where we used Eq. (1.25) to introduce the superfluid velocity and Eq. (2.1) to switch to momentum space. The last transformation simply corresponds to a shift of the $\boldsymbol{k}$-vector. The bare-particle energies can then be Taylor-expanded around $\boldsymbol{k}$. Introducing small superfluid velocities in the individual boson components therefore leads to a change in momentum and energy

$$\begin{aligned} &\boldsymbol{k} \to \boldsymbol{k} - m_\alpha \boldsymbol{v}_{s\alpha}, \\ &\epsilon^\alpha_{\boldsymbol{k}} \to \epsilon^\alpha_{\boldsymbol{k}} - m_\alpha \boldsymbol{v}_{s\alpha} \cdot \boldsymbol{\nabla}_{\boldsymbol{k}} \epsilon^\alpha_{\boldsymbol{k}} + \mathcal{O}(v^2_{s\alpha}). \end{aligned} \tag{2.22}$$

We expand the bare-particle energies only to linear order in $\boldsymbol{v}_{s\alpha}$ since we are only interested in the term of the free energy that is bilinear in the two superfluid velocities.

To find the expansion of the excitation spectrum $\mathcal{E}_{\boldsymbol{k}\sigma}$, we expand the characteristic polynomial of $\mathcal{M}_{\boldsymbol{k}}\sigma_3$ in powers of $\boldsymbol{v}_{s\alpha}$ along the lines of Ref. 33. We can then evaluate the free energy given by Eq. (2.19). Comparison to Eq. (1.20) leads to the following superfluid-drag coefficient (a derivation is given in Appendix B.3)

$$\rho_d = \frac{1}{\mathcal{V}} {\sum_{\boldsymbol{k}}}' \frac{2m_A m_B F_{AB}^2 \epsilon^A_{\boldsymbol{k}} \epsilon^B_{\boldsymbol{k}}}{\mathcal{E}^0_{\boldsymbol{k}+}\mathcal{E}^0_{\boldsymbol{k}-}\left[\mathcal{E}^0_{\boldsymbol{k}+} + \mathcal{E}^0_{\boldsymbol{k}-}\right]^3} \left(\partial_{k_u}\epsilon^A_{\boldsymbol{k}}\right)\left(\partial_{k_u}\epsilon^B_{\boldsymbol{k}}\right), \tag{2.23}$$

where $\hat{\boldsymbol{u}}$ denotes the direction of the superfluid flow (the two components are assumed to flow in the same direction), $\partial_{k_u} \equiv \hat{\boldsymbol{u}} \cdot \boldsymbol{\nabla}_{\boldsymbol{k}}$ and $\mathcal{E}^0_{\boldsymbol{k}\sigma}$ is the excitation spectrum for the two components at rest, given by Eq. (2.16). The denominator in the last expression penalizes $\boldsymbol{k}$-states corresponding to high energies, such that only states which have a realistic probability of being occupied make a relevant contribution to the drag at $T = 0$.

The superfluid drag is independent of the sign of the interspecies interaction and vanishes if it goes to zero or if one of the particle densities or masses goes to zero. Since the excitation spectrum itself depends on the interaction parameters, the masses, and the bare-particle bandstructures, the drag depends on these quantities in a non-trivial way. However, at least when these quantities are small, one can say that the drag increases with increasing interspecies interactions and with the particle masses. It also increases with the bare-particle bandwidth which is a measure of the kinetic energy and manifests itself in the above expression via the bandstructure and its directional derivative. These observations are consistent with the physical picture, where a particle of one component is being dressed by particles of the other component; the drag is more efficient when the interaction between the two components is stronger or when their mobility is higher. With increasing masses, more mass density gets dragged along, leading to an enhanced drag.

Chapter 3

Numerical evaluation of the superfluid drag

We evaluate the superfluid-drag coefficient for different, experimentally implementable lattice geometries in two dimensions. In contrast to Ref. 5, where this has been done for the three dimensional cubic lattice using the tight-binding approximation, we calculate the bandstructures and Hubbard-interaction parameters numerically. This allows us to probe weak lattice potentials, where to our knowledge the physics of the drag has not been investigated so far. Some considerations about the numerical procedures described in this chapter are discussed in Appendix C. For simplicity, the index α is omitted in this chapter whenever single-species properties are discussed.

3.1 Calculation of the bandstructures

The bandstructure illustrates the energy eigenstates of a single particle in the lattice. In order to diagonalize the single-particle Hamiltonian numerically, we expand it in plane waves and truncate it to an operator of finite dimensionality. The numerical diagonalization procedure was carried out using the EISPACK library [34].

In a periodic potential $V(\boldsymbol{r})$, the single-particle Hamiltonian reads (omitting the chemical potential which we assume to be a constant)

$$H_1 = -\frac{1}{2m}\left(\frac{\partial^2}{\partial x^2} + \frac{\partial^2}{\partial y^2}\right) + V(\boldsymbol{r}), \tag{3.1}$$

with eigenfunctions given by the well known Bloch states

$$\Psi_{n\boldsymbol{k}}(\boldsymbol{r}) = \frac{1}{\sqrt{\mathcal{V}}}\, e^{i\boldsymbol{k}\cdot\boldsymbol{r}} u_{n\boldsymbol{k}}(\boldsymbol{r}), \tag{3.2}$$

where the quantum number $\boldsymbol{k}$ runs over all allowed values in the first Brillouin zone and n denotes the discrete band index. The function $u_{n\boldsymbol{k}}(\boldsymbol{r})$ has the same periodicity

as the lattice and can therefore be expanded in Fourier coefficients, corresponding to different reciprocal-lattice vectors $\boldsymbol{G}' \in \mathbb{G}$

$$u_{n\boldsymbol{k}}(\boldsymbol{r}) = \sum_{\boldsymbol{G}' \in \mathbb{G}} C_{n\boldsymbol{k},\boldsymbol{G}'} e^{i\boldsymbol{G}'\cdot\boldsymbol{r}}, \tag{3.3}$$

whereby the following relation holds

$$\sum_{\boldsymbol{G} \in \mathbb{G}} \left| C_{n\boldsymbol{k},\boldsymbol{G}} \right|^2 = 1. \tag{3.4}$$

The Bloch eigenvalue problem thus assumes the form

$$H_1 \sum_{\boldsymbol{G}' \in \mathbb{G}} C_{n\boldsymbol{k},\boldsymbol{G}'} \left| \boldsymbol{k} + \boldsymbol{G}' \right\rangle = \varepsilon_{n\boldsymbol{k}} \sum_{\boldsymbol{G}' \in \mathbb{G}} C_{n\boldsymbol{k},\boldsymbol{G}'} \left| \boldsymbol{k} + \boldsymbol{G}' \right\rangle, \tag{3.5}$$

where $|\boldsymbol{k}\rangle$ is shorthand for $\mathcal{V}^{-1/2} e^{i\boldsymbol{k}\cdot\boldsymbol{r}}$. Applying $\langle \boldsymbol{k} + \boldsymbol{G}|$ on the above equation and using the orthonormality of the plane-wave basis leads to the eigenvalue equation

$$\sum_{\boldsymbol{G}' \in \mathbb{G}} \underbrace{\left\langle \boldsymbol{k} + \boldsymbol{G} \right| H_1 \left| \boldsymbol{k} + \boldsymbol{G}' \right\rangle}_{(H_{\boldsymbol{k}})_{\boldsymbol{G},\boldsymbol{G}'}} C_{n\boldsymbol{k},\boldsymbol{G}'} = \varepsilon_{n\boldsymbol{k}} C_{n\boldsymbol{k},\boldsymbol{G}} \,. \tag{3.6}$$

The bandstructure $\varepsilon_{n\boldsymbol{k}}$ and the plane-wave coefficients $C_{n\boldsymbol{k},\boldsymbol{G}}$, can therefore be obtained by diagonalizing the matrix $H_{\boldsymbol{k}}$.

Finite dimensionality of this eigenvalue problem is achieved by taking into account only a finite number of reciprocal-lattice vectors $N_{\boldsymbol{G}}$. In our case, $N_{\boldsymbol{G}} \gtrsim 100$ leads to the requisite numerical precision in the energies and Bloch functions of the lowest band for all the lattices. Note that the number of reciprocal-lattice vectors determines the number of bands the calculation obtains. To resolve the higher bands, one would therefore need to take into account a higher number of reciprocal-lattice vectors.

The diagonal matrix elements of $H_{\boldsymbol{k}}$ can directly be calculated using the identity

$$\frac{1}{\mathcal{V}} \int d\boldsymbol{r}\, e^{i\boldsymbol{k}\cdot\boldsymbol{r}} = \delta_{\boldsymbol{k},0} \,, \tag{3.7}$$

which leads to

$$\left\langle \boldsymbol{k} + \boldsymbol{G}_{l,p} \right| H_1 \left| \boldsymbol{k} + \boldsymbol{G}_{l,p} \right\rangle = \frac{1}{2m} \left| \boldsymbol{k} + \boldsymbol{G}_{l,p} \right|^2, \tag{3.8}$$

where the integers l, p denote the expansion of $\boldsymbol{G}$ in the reciprocal-lattice basis vectors

$$\boldsymbol{G}_{l,p} = l\boldsymbol{b}_1 + p\boldsymbol{b}_2 \,. \tag{3.9}$$

The diagonal matrix elements for the different lattices are explicitly given in Appendix A. The off-diagonal matrix elements can also easily be calculated and read

$$\begin{aligned}
\left\langle \boldsymbol{k} + \boldsymbol{G}_{l_1,p_1} \right| H_1 \left| \boldsymbol{k} + \boldsymbol{G}_{l_2,p_2} \right\rangle &= \left\langle \boldsymbol{k} + \boldsymbol{G}_{l_1,p_1} \right| V(\boldsymbol{r}) \left| \boldsymbol{k} + \boldsymbol{G}_{l_2,p_2} \right\rangle, \\
\left\langle \boldsymbol{k} + \boldsymbol{G}_{l_1,p_1} \right| V^{\mathrm{3B}}(\boldsymbol{r}) \left| \boldsymbol{k} + \boldsymbol{G}_{l_2,p_2} \right\rangle &= \frac{V_0}{4} \Big(\delta_{l_1,l_2\pm1} \delta_{p_1,p_2} + \delta_{l_1,l_2} \delta_{p_1,p_2\pm1} + \delta_{l_1,l_2\pm1} \delta_{p_1,p_2\pm1} \Big), \\
\left\langle \boldsymbol{k} + \boldsymbol{G}_{l_1,p_1} \right| V^{\mathrm{4B}}(\boldsymbol{r}) \left| \boldsymbol{k} + \boldsymbol{G}_{l_2,p_2} \right\rangle &= \frac{V_0}{4} \Big(\delta_{l_1,l_2\pm1} \delta_{p_1,p_2} + \delta_{l_1,l_2} \delta_{p_1,p_2\pm1} \Big),
\end{aligned} \tag{3.10}$$

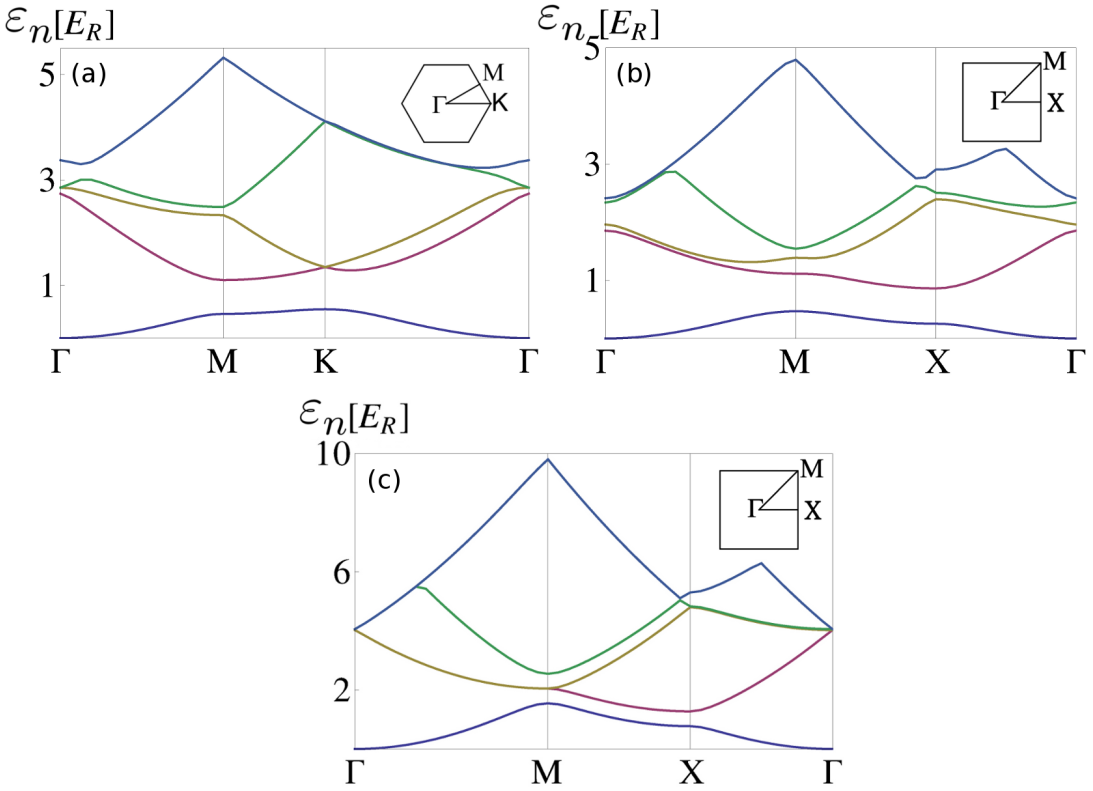

Figure 3.1: Numerically calculated band structures along points of high symmetry, with a light-shift strength parameter $V_0/E_R = -1$, showing the first 5 bands. (a) Bandstructure for the 3BTL in agreement with the one presented in [9]. (b) Bandstructure for the 3BSL and (c) for the 4BSL. The insets show the points of high symmetry in the respective Brillouin zones.

where the respective potentials are given by Eqs. (1.29, 1.32). Note that for the 3BLs only the diagonal and not the off-diagonal matrix elements depend on the specific lattice geometry. Furthermore, all the matrix elements are real quantities which makes $H_{\boldsymbol{k}}$ a symmetric matrix. The numerical diagonalization procedure for $N_{\boldsymbol{G}} = 121$ obtains the bandstructures depicted in Fig. 3.1.

The bands of the 4BSL are much broader than the ones of the 3BLs (note the different scale). This implies that the atoms have a higher mobility in this lattice. Since the drag increases with the kinetic energy [cf. Eq. (2.23)], the effect is more pronounced in the 4BSL than in the other lattice geometries. This is partly due to the smaller lattice spacing of the 4BSL (see Fig. 1.3) and consistent with the fact that the SF-MI transition happens at around $|V_0| = 10\, E_R$ for this potential whereas it occurs already at around $|V_0| = 4\, E_R$ for the 3BLs. Furthermore, Fig. 3.1 (c) shows that the single-band approximation, Eq. (1.35), is not a good approximation for the 4BSL at lattice depths as shallow as $|V_0| = 1\, E_R$, because the lowest and the first excited bands have an energy overlap. However, since all the interesting physics happens at deeper lattices for the 4BSL, our findings are not based on results obtained at such shallow lattices.

Comparing Figs. 3.1 (b) and (c) shows that some degeneracies which are present in the square lattice produced by four laser beams are lifted in the one created by three laser beams (e.g. in first and second excited bands between the Γ and the M point). This is related to the lower symmetry in the 3BSL compared to the 4BSL. Whereas the 4BSL is symmetric under rotation of 90°, the 3BSL is only symmetric under rotation of 180°.

3.2 Calculation of the Hubbard-interaction parameters

Since we are only interested in the lowest band, we omit the band index in this subsection. In order to calculate the Hubbard-interaction parameters, Eq. (1.39), one has to construct localized Wannier functions by an appropriate superposition of Bloch waves. The latter are determined through the plane-wave coefficients $C_{\boldsymbol{k},\boldsymbol{G}}$, obtained by the EISPACK routine. Their following relationships have been numerically confirmed up to an acceptable precision [$\delta_{\boldsymbol{k},\boldsymbol{k}'}$ only holds if $\boldsymbol{k}$ and $\boldsymbol{k}'$ are sufficiently far apart from each other and $\mathcal{O}(10^{-2})$ terms are neglected]

$$\begin{aligned} &\Psi_{\boldsymbol{k}}(\boldsymbol{r}) = \Psi_{\boldsymbol{k}+\boldsymbol{G}}(\boldsymbol{r}) \quad \text{for} \quad \boldsymbol{G} \in \mathbb{G}, \\ &\int_{\mathcal{V}} d\boldsymbol{r} \Psi^*_{\boldsymbol{k}}(\boldsymbol{r}) \Psi_{\boldsymbol{k}'}(\boldsymbol{r}) = \delta_{\boldsymbol{k},\boldsymbol{k}'}. \end{aligned} \tag{3.11}$$

Here the volume $\mathcal{V}$ is N times the volume of the Wigner-Seitz cell and N is the number of $\boldsymbol{k}$-values included in the calculation.

The Wannier function centered around the lattice site $\boldsymbol{R}$ is given by

$$W(\boldsymbol{r}-\boldsymbol{R}) = \frac{1}{\sqrt{N}} \sum_{\boldsymbol{k}} e^{-i\boldsymbol{k}\cdot\boldsymbol{R}} \Psi_{\boldsymbol{k}}(\boldsymbol{r}). \tag{3.12}$$

Because for each value of $\boldsymbol{k}$, the Bloch function is only defined up to an overall phase, the above definition of the Wannier function is not unique. One therefore has to choose a gauge

$$\Psi_{\boldsymbol{k}} \to e^{i\phi(\boldsymbol{k})} \Psi_{\boldsymbol{k}}, \tag{3.13}$$

which leads to localized Wannier functions. This problem has been discussed by Kohn for an isolated band in a one dimensional potential with inversion symmetry [35] and by des Cloizeaux for the more general case of a multidimensional potential with inversion symmetry [36]. A summary of their findings can be found in Ref. 37. The problem essentially boils down to finding a gauge for which the Bloch functions are continuous not only for $\boldsymbol{k} \in \mathbb{R}$ but also in a strip of the complex plane $|\mathrm{Im}\{\boldsymbol{k}\}| < A$, for some finite and positive A. A recipe for finding this gauge is given in Ref. 37 and a program which finds the maximally localized Wannier functions by minimizing their spread was developed by Marzari *et al.* [38, 39].

Here a much simpler gauge transformation [40] was used

$$\Psi_{\boldsymbol{k}}(\boldsymbol{r}) \to \exp\left[-i\mathrm{Im}\{\ln \Psi_{\boldsymbol{k}}(0)\}\right] \Psi_{\boldsymbol{k}}(\boldsymbol{r}). \tag{3.14}$$

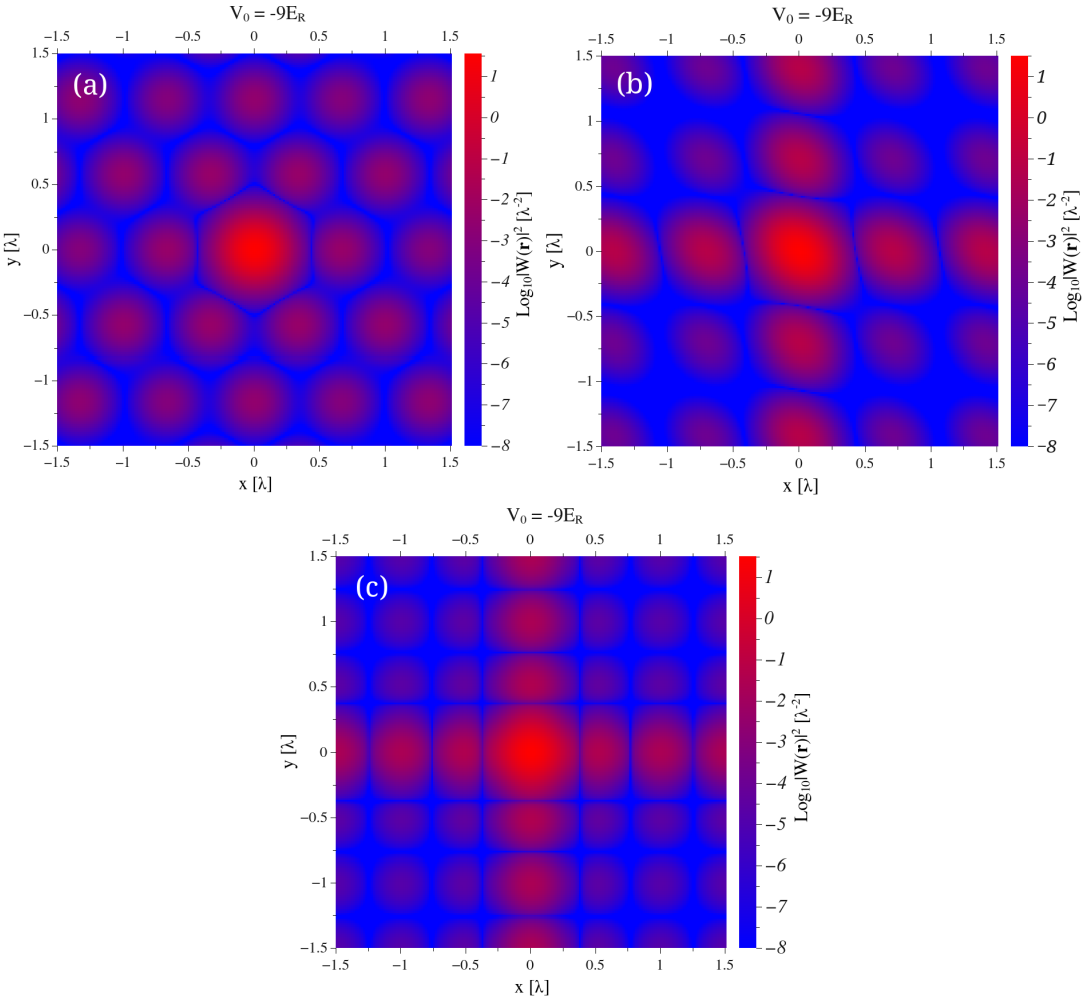

Figure 3.2: Numerically calculated Wannier functions at $\boldsymbol{r} = 0$ for $V_0/E_R = -9$. (a) 3BTL, (b) 3BSL, and (c) 4BSL.

This transformation does not lead to the maximally localized Wannier functions, which decay exponentially as $\boldsymbol{r} \to \infty$. However, by constructing Bloch functions which all have the same phase at $\boldsymbol{r} = 0$, this procedure results in Wannier functions that are sufficiently localized to neglect inter-site interactions. The Wannier functions are shown in Fig. 3.2 and their orthonormality relation was numerically reproduced [neglecting $\mathcal{O}(10^{-2})$ terms]

$$\int_{\mathcal{V}} d\boldsymbol{r} W^*(\boldsymbol{r} - \boldsymbol{R}) W(\boldsymbol{r} - \boldsymbol{R}') = \delta_{\boldsymbol{R},\boldsymbol{R}'}. \tag{3.15}$$

Because the Wannier functions are fairly localized, the volume of integration can be reduced drastically without affecting the results in a notable way. Since the absolute value squared of the Wannier functions on the closest neighboring sites is about two orders of magnitude lower than their maximum value (this also holds for lattices as shal-

low as $|V_0| = 1\,E_R$), nearest-neighbor interactions are about two orders of magnitude lower than on-site interactions and can safely be neglected [cf. Eq. (1.39)].

To derive the superfluid drag in the experimentally relevant case of a quasi two-dimensional system, one should start with the three-dimensional Hamiltonian and integrate out the third dimension in accordance with the experimental way of implementing the quasi two-dimensionality. Motivated by recent experiments [9], we choose a one-dimensional optical lattice in the z-direction for this purpose. The resulting transverse potential reads $V(z) = V_z \sin^2(k_L z)$ and is created by a laser of the same wavelength as used for the in-plane lattice with an increased light-shift strength parameter $V_z = 30E_R$. This makes the lattice sufficiently deep to cut the system into slices which are decoupled, such that in each of the slices the degrees of freedom in the z-direction are frozen and the dynamics is two-dimensional. As explained in Appendix D, the only consequence relevant for the superfluid drag is a modification of the Hubbard-interaction parameter.

Approximating the confining potential around one of the minima leads to a harmonic potential with mass dependent frequency $\omega_z = \sqrt{2V_z k_L^2/m}$. If the scattering lengths are small compared to the corresponding oscillator length $l_z = \sqrt{1/m\omega_z}$, we can assume that the two-body collisions are not affected by the confinement and Eq. (1.39), with three-dimensional Wannier functions, gives the correct interaction parameters $U_{\alpha\beta}$. In our case, this condition is readily fulfilled; for ^{87}Rb: $l_z \approx 70\,\mathrm{nm}$ and $a_s \approx 5\,\mathrm{nm}$. In order to derive an expression in terms of the numerically calculated two-dimensional Wannier functions, we write their three-dimensional counterparts as a product of an in-plane part and a Gaussian in the z-direction (cf. App. D)

$$W_\alpha(\boldsymbol{r}, z) = W_\alpha(\boldsymbol{r}) \left(\frac{m_\alpha \omega_{z\alpha}}{\pi}\right)^{1/4} \exp\left(-\frac{m_\alpha \omega_{z\alpha}}{2} z^2\right), \tag{3.16}$$

where $\boldsymbol{r}$ is a two-dimensional vector and we only distinguish between two- and three-dimensional Wannier functions by their arguments. Here we have reintroduced the index α to stress their dependence on the component mass. The z-dependence of $U_{\alpha\beta}$ can then easily be integrated out and we are left with

$$U_{\alpha\beta} = \gamma_{\alpha\beta} \sqrt{\frac{m_\alpha \omega_{z\alpha} m_\beta \omega_{z\beta}}{\pi(m_\alpha \omega_{z\alpha} + m_\beta \omega_{z\beta})}} \int d\boldsymbol{r}\, |W_\alpha(\boldsymbol{r})|^2 \left|W_\beta(\boldsymbol{r})\right|^2. \tag{3.17}$$

The two-dimensional Wannier functions $W(\boldsymbol{r})$ are illustrated in Fig.3.2. By evaluating the last expression, we were able to reproduce the dependence of the interaction parameter on the lattice depth calculated by Blakie and Clark [8], depicted in Fig. 1.4.

Chapter 4

Results

In the following, we present our findings for the superfluid drag in different lattice geometries, for weak and strong interspecies scattering. To obtain a dimensionless quantity, we normalize the superfluid drag by $\rho_A = N_A m_A/\mathcal{V}$. Superfluidity at all lattice depths is assured by choosing an incommensurate filling $n_A = n_B = \sqrt{2}$. The intraspecies scattering lengths are set to $a_{AA} = 100\, a_0$ (a_0 is the Bohr radius) and $a_{BB} = 65\, a_0$. For all the lattices we choose the superfluid flows to be co-directed in the x-direction defined in Fig. 1.3. For the laser wavelength, which determines the lattice spacing, we choose $\lambda_L = 1064$ nm. The results obtained for the superfluid drag are shown in Fig. 4.1. Figures (a), (c), and, (e) correspond to weak interspecies interactions and Figs. (b), (d), and, (f) to strong ones, just before phase separation occurs [i.e., just before the inequality (1.40) is violated].

Qualitatively, all the lattices show a similar behavior in the superfluid drag for both weak and strong interspecies interactions. Quantitatively however, Fig. 4.1 shows that the drag is much more pronounced for strong interspecies interactions in all the lattices, consistent with the discussion at the end of Ch. 2. To illustrate the qualitative behavior of the superfluid drag, Fig. 4.2 shows cuts through Fig. 4.1 (b) for experimentally relevant mass ratios. For a fixed mass ratio, the drag increases upon raising $|V_0|$ from zero, reaches its maximum and then decreases. A similar behavior can be observed when increasing the mass ratio at a fixed lattice depth. This non-monotonic dependence on the lattice depth emerges from an interplay of the kinetic and interaction energies. On the one hand, Eq. (2.23) shows that the interspecies interactions give a quadratic contribution to the superfluid drag. However, increasing the (inter- and intraspecies) interactions also increases the quasiparticle energies in the denominator which decreases the drag. On the other hand, the bare particle energies and their derivatives in the numerator of Eq. (2.23) imply that the drag grows with the kinetic energy. The behavior of the interaction and kinetic energies when increasing the lattice depth are illustrated in Fig. 1.4. In a shallow lattice, the kinetic energy is high and the interaction energy low since the particles are fairly delocalized. Upon increasing the lattice depth, the atoms get confined at their sites, leading to reduced tunneling and an enhanced on-site interaction.

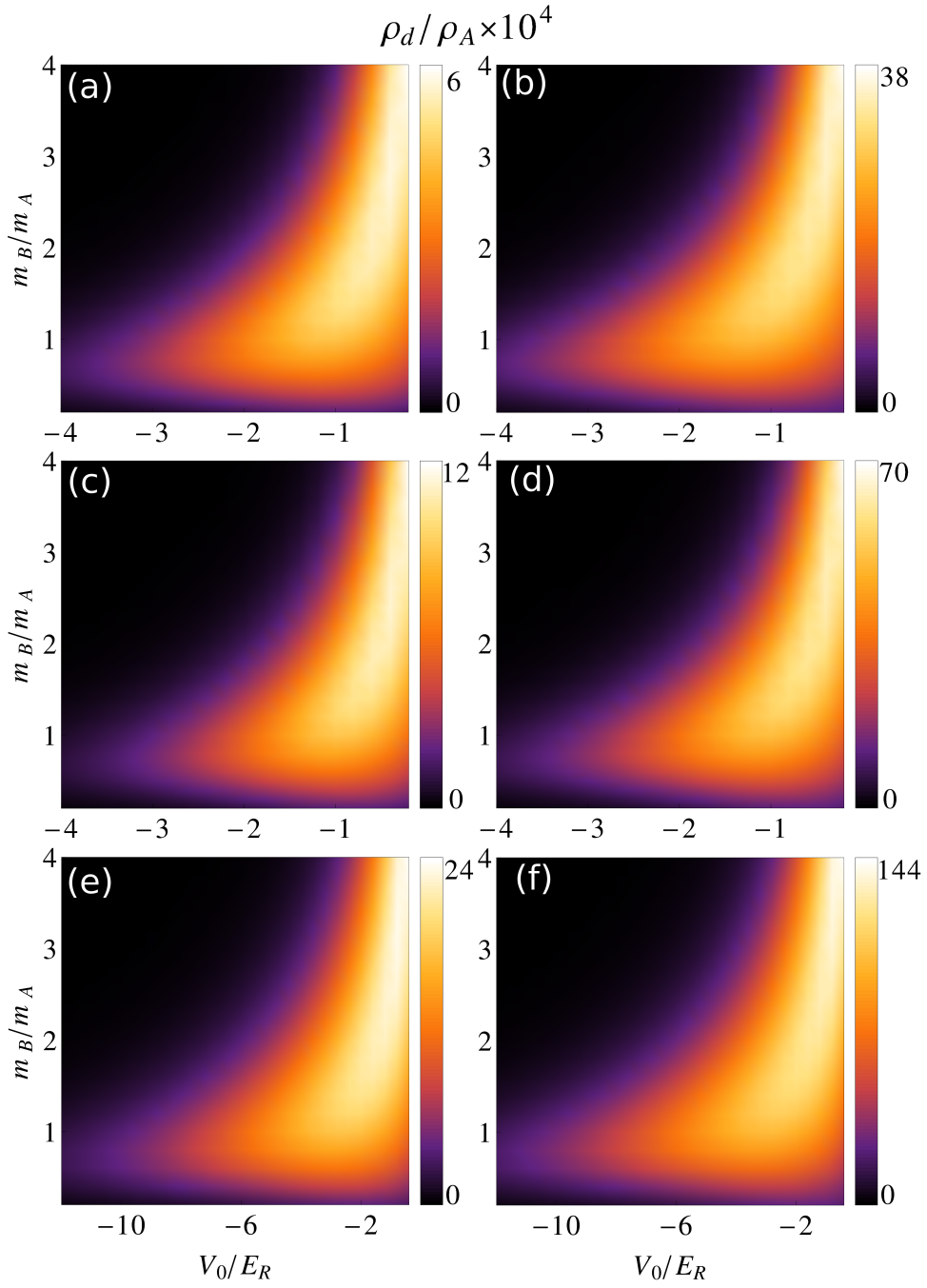

Figure 4.1: Superfluid drag for different lattices and interaction strengths: (a) and (b) three-beam triangular lattice (3BTL), (c) and (d) three-beam square lattice (3BSL), (e) and (f) four-beam square lattice (4BSL). The left column [(a), (c), (e)] corresponds to weak interspecies interactions $a_{AB} = 30\,a_0$, the right column [(b), (d), (f)] to strong ones $a_{AB} = 64\,a_0$. Note the different scales for the color scheme.

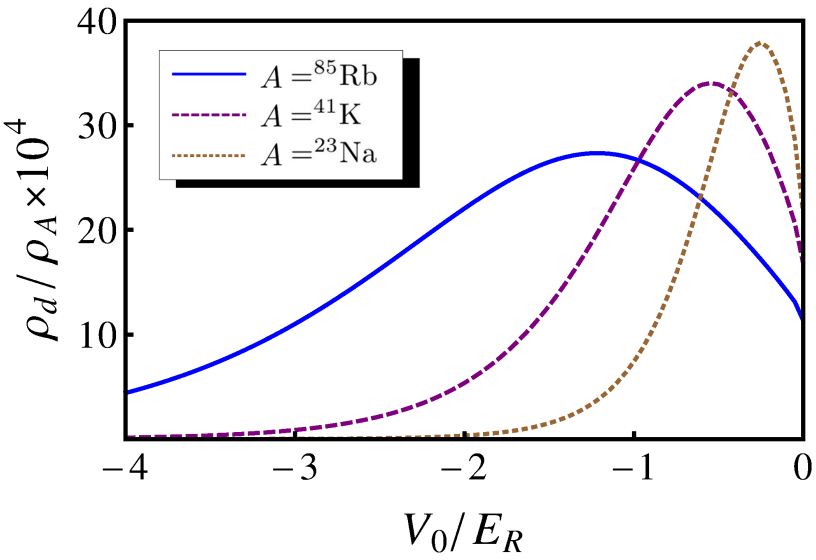

Figure 4.2: Superfluid drag in a 3BTL as a function of the lattice depth V_0 for fixed mass ratios corresponding to the mixtures ^{87}Rb-^{85}Rb ($m_B/m_A \approx 1$, solid), ^{87}Rb-^{41}K ($m_B/m_A \approx 2.2$, dashed) and ^{87}Rb-^{23}Na ($m_B/m_A \approx 3.8$, dotted). Component B corresponds to ^{87}Rb in all three cases. The interspecies scattering length is set to $a_{AB} = 64\, a_0$.

For a shallow lattice, the drag shows a growth with increasing $|V_0|$, which results from the increasing interspecies interaction [cf. Fig. 1.4 (b)], for a deep lattice potential the drag shows an exponential decay due to the suppressed kinetic energy [cf. Fig. 1.4 (a)]. When assuming the normalization ρ_A to be constant, increasing the mass ratio only increases m_B. The non-monotonic dependence of the drag on the mass ratio then results from the linear dependence of the numerator on m_B and the reduced kinetic energy for high masses. The fact that the similar dependence on the lattice depth and the mass ratio is a general feature of the drag explains its qualitative similarity for different lattices and interaction strengths.

In a more general way [i.e. without using Eq. (2.23)] this similarity can be explained by the behavior of the relative lattice depths V_0/E_R^α. As discussed in Appendix C.3, it is this quantity which defines the single-particle states. The recoil energy merely rescales the energy of these states [cf. Eq. (C.9)]. On increasing $|V_0|$, the relative lattice depths for both components increase, while for increasing m_B/m_A, only the relative lattice depth of component B increases when keeping E_R^A constant. This implies a similar behavior of the drag on the lattice depth and the mass ratio.

When interchanging the labels of the two components, the drag should of course be invariant which means that its values at m_B/m_A and m_A/m_B are connected by some mapping procedure. Interchanging all the component-dependent quantities yields

$$\frac{\rho_d}{\rho_0}\left(\frac{m_B}{m_A}, \frac{V_0}{E_R^A}\right) = \frac{m_B}{m_A}\frac{\rho_d}{\rho_0}\left(\frac{m_A}{m_B}, \frac{m_B}{m_A}\cdot\frac{V_0}{E_R^A}\right), \tag{4.1}$$

which is fulfilled in the above plots.

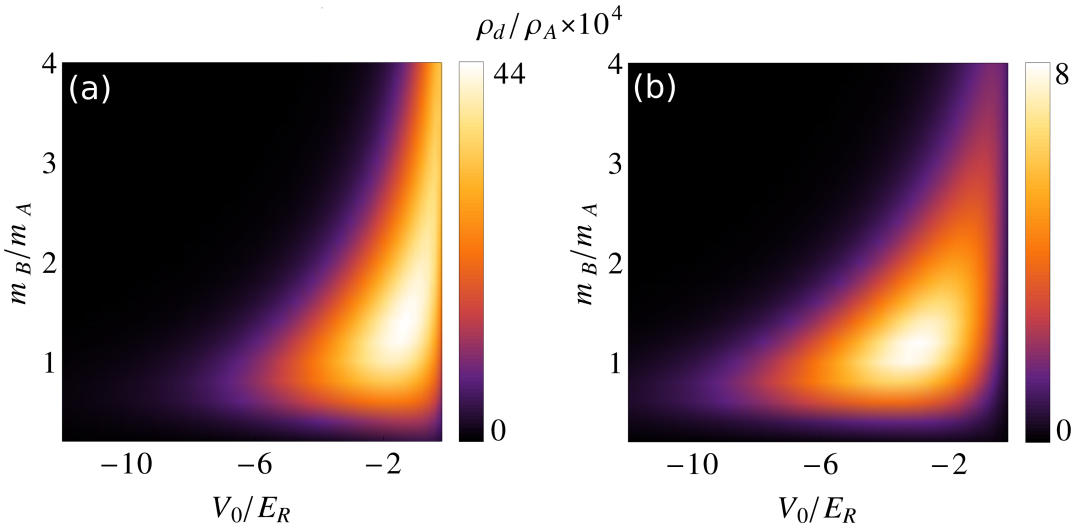

Figure 4.3: Superfluid drag for the cubic lattice using tight-binding and the harmonic approximation in (a) two dimensions (4BSL) and (b) three dimensions. The interspecies scattering length is $a_{AB} = 64\, a_0$.

In contrast to the results of Ref. 5, we find that the mass ratio which maximizes the drag depends on the lattice depth, varying significantly from unity as one goes to shallower lattices ($|V_0| \lesssim 1\, E_R$ for the 3BLs). For a shallow lattice, a high mass ratio seems to be favorable for the drag as illustrated in Fig. 4.2. For lattices deeper than $|V_0| \approx 1.2\, E_R$, our results agree with Ref. 5 and we find the optimal mass ratio to be unity. This mismatch for weak lattice potentials is not due to our different numerical approach but because of a mistake in Eq. (53) in Ref. 5, which leads to tunneling amplitudes that decay much too fast with the lattice depth. The deviation from an optimal mass ratio equal to one is then only visible at a much shallower lattice, where they did not discuss their results because of the questionable validity of the tight-binding approximation. To confirm this, we plotted the drag for the cubic lattice in two and three dimensions in the tight-binding, i.e. only nearest neighbor hopping, and the harmonic approximation where the Wannier functions are the Gaussian groundstates for the quadratically approximated lattice sites (see Fig. 4.3). As expected, the mass ratio which maximizes the drag differs from unity at shallow lattices in accordance with our numerical approach.

Although the qualitative behavior of the drag seems to be very general, there are significant quantitative differences in the lattice geometries. Comparing the 3BSL with the 4BSL, one notices that in the 4BSL the superfluid drag is much larger over a broader range of lattice depths. This is because of the higher kinetic energy in the 4BSL which was already observed in the bandstructures in Sec. 3.1. Figure 1.4 shows that for the 4BSL, the kinetic energy decreases much slower with the lattice depth compared to the 3BLs, while the Hubbard-interaction parameters increase the same for all lattices. Since the drag increases with both the kinetic and the interaction energy, it is much

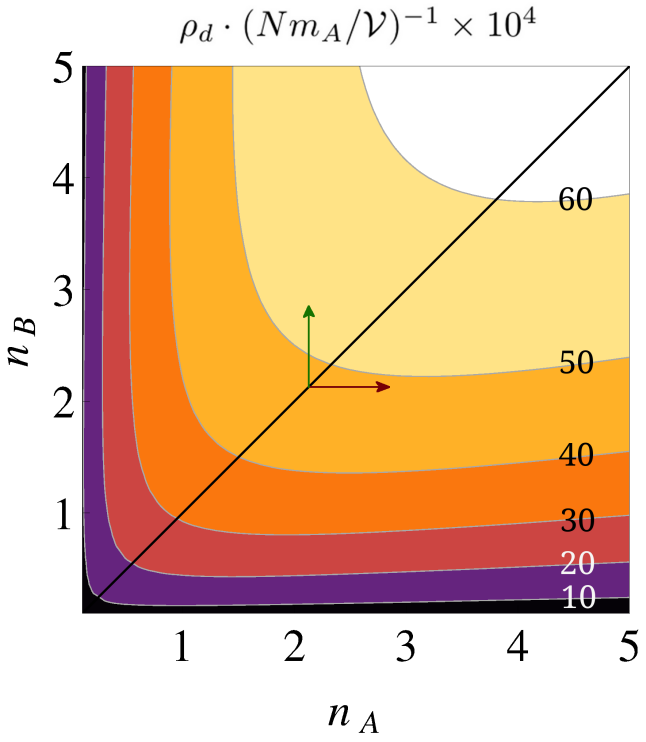

Figure 4.4: Superfluid drag in a 3BTL (*not* normalized with n_A) as a function of the particle densities for $A = {}^{85}$Rb and a lattice depth $V_0 = -1.2\, E_R$ which maximizes the drag for this mass ratio (see Fig. 4.2). The other parameter values are the same as in Fig. 4.1 (b). The arrows denote what happens to the drag when increasing either one of the particle densities. The slope along the density of the more weakly interacting component (here component B, green arrow) turns out to be always larger then the slope along the density of the more strongly interacting component (here component A, red arrow).

more pronounced in the 4BSL than in the 3BLs.

A possible explanation as to why the drag is stronger in the 3BSL than in the 3BTL can be given if one envisions the drag as being mediated by component A particles, dressed by a cloud of component B particles and vice versa. In this case one could argue that the higher coordination number of the 3BTL leads to more events whereby one of the particles within the cloud splits off the dressed particle.

In the tight-binding approximation (cf. Fig. 4.3), the quantitative value for the drag in the 4BSL is almost an order of magnitude smaller than what our numerical approach produced. This probably results from our Wannier functions, which of course are much less localized than Gaussians, and from the fact that we include hopping to arbitrary lattice sites. In three dimensions, we find a much smaller drag as compared to two dimensions. This is because the localization in one dimension increases the interspecies interaction, without having an important influence on the mobility of the atoms in the plane. Furthermore, as in the 3BTL, the increased coordination number possibly leads to a reduced drag.

In Fig. 4.4, the superfluid drag is shown in dependence of the densities of the two components. We choose $Nm_A/\mathcal{V}$ for the normalization constant, such that it is independent of the densities. Although the drag varies with the densities, the curves in Fig. 4.2 only get shifted in the vertical direction upon changing them. This implies that for a fixed mass ratio, the lattice depth V_0 which maximizes the drag is independent of the particle densities n_α and therefore a function of the mass ratio and the scattering lengths only. The dependence of the drag on the densities, Fig. 4.4, varies significantly when changing the mass ratio or the lattice depth. However, comparing the density dependence at the lattice depths which maximize the drag for the respective mass ratios, we find that it hardly changes at all.

Furthermore, we note that for two components with the same scattering length and mass, the density dependence has a mirror symmetry along the diagonal (there is nothing that distinguishes the two components). Since the density dependence does not change from one mass ratio to the other, when comparing it at lattice depths which maximize the drag, this symmetry occurs for all mass ratios when the scattering lengths are equal and the lattice depth is set to maximize the drag. Finally, we found that the drag always increases upon increasing the particle numbers when $n_A \approx n_B$. For two species with different scattering lengths, increasing the number of the more weakly interacting particles always seems to be more favorable (see arrows in Fig. 4.4).

Chapter 5

Conclusions and outlook

We have studied the superfluid drag between the components of a two-species BEC in optical lattices. For this purpose, we have generalized an expression for the superfluid-drag coefficient to an arbitrary lattice geometry. This expression gives some insight in the general behavior of the drag on various parameters, such as the interaction and kinetic energies. We have evaluated this expression for different lattice geometries using a numerically exact approach to calculate the bandstructures and Hubbard-interaction parameters. This assures that our results are valid until the lattice depths become so shallow that the single-band approximation fails ($< 1\, E_R$ for the 3BLs). To clarify the dependence of the superfluid drag on the lattice geometry, we have presented results for rectangular and non-rectangular lattices with separable and non-separable potentials.

We have found the qualitative behavior of the drag to be very general. As expected, the drag increases with kinetic energy, since it is easier to drag along mobile atoms, as well as with the interspecies interaction energy which is the source of the superfluid drag. These two effects lead to a non-monotonic dependence of the drag on the lattice depth V_0: upon increasing the lattice depth from zero, the drag increases due to the increasing interspecies interaction, then it reaches its maximum and finally it decreases with increasing $|V_0|$ because of the reduction in the kinetic energy.

In contrast to previous findings [5], we found the mass ratio which maximizes the drag to be dependent on the lattice depth. Our tight-binding calculations show that this discrepancy is not due to our numerical approach but emerges from a mistake in their work. The tight-binding calculations also imply that the drag is enhanced with reduced dimensionality because the confinement increases the interspecies interaction energy.

Quantitatively, the drag varies with the lattice geometry. The 4BSL has the largest drag because the atoms have an increased kinetic energy as compared to the other lattices. In the 3BTL the drag is the lowest, which might be because of its higher coordination number. A decrease in drag with an increase in the coordination number is also consistent with the low drag in three dimensions.

Finally, we have also examined the dependence of the drag on the component densities and have found the lattice depth which maximizes the drag for a given mass ratio

to be independent of the densities. Furthermore, it seems to be always more favorable to increase the density of the more weakly interacting particles, which could be an advantage in drag experiments since the more strongly interacting particles are usually lost more easily in the preparation process.

Here we have only investigated the superfluid drag for the case of co-directed superflows in the x-direction. It would be interesting to generalize this work to other directions, as well as to superflows which are not co-directed. In the latter case however, our expression for the drag, Eq. (2.23), does not hold anymore. Since the drag in a lattice in general depends on both of the flow directions, it might be best represented by a tensor, where the indices denote the superfluid directions.

Another continuation of this work would be the investigation of superfluid drag in the strong interaction limit. This would be particularly interesting since in the limit of hardcore intraspecies and softcore interspecies interactions, a negative drag was found by means of Monte Carlo simulations [7]. An analytic expression for the drag in the limit of strong interactions could maybe shed some light on this change of sign, which possibly implies a vanishing drag at some point in parameter space. Since the Bogoliubov approximation only works for weak interactions, one would have to use a different method for solving the Hamiltonian. Some efforts in this direction using a Gutzwiller-mean field approach unfortunately were unfruitful. This approach is not suitable because it neglects terms where tunneling of both species occurs, which are the source of the superfluid drag.

Another intriguing challenge would be to come up with a scheme to measure the drag coefficient. In order to achieve this, one would need to be able to fix both superfluid velocities at different values. For measuring the superfluid density in ultracold atoms, a scheme exists which uses light of non-vanishing angular momentum to introduce the superfluid velocity [25]. Although this has not been experimentally realized so far, one could maybe generalize the scheme to the two-species case and thus come up with a way to measure the drag. Another possibility would be to utilize the above mentioned point of vanishing drag once one understands its origin and location in parameter space.

Although the superfluid drag seems to be not a particularly tangible quantity, we hope that our study will motivate drag experiments with ultracold atoms in optical lattices.

Acknowledgements

I would like to thank my direct supervisor, Vladimir M. Stojanović, on whose ideas this whole work is based. Not only did he discuss with me many fundamental issues in the underlying physics but he also invested a lot of time in teaching me how to write a scientific paper and gave me helpful advice for my future career.

Many thanks also to Christoph Bruder who offered me the opportunity for this thesis and spent a lot of time discussing different aspects of the work in some detail. Also for his invaluable help in applying for a PhD position I am very grateful.

For fruitful discussions about the basics of ultracold atoms, I would like to thank Andreas Wagner.

Appendix A

Optical lattice potentials

A.1 The three-beam triangular lattice

A 3BTL is created if the three laser beams mutually enclose angles of 120°

$$\theta_1 = 0, \qquad \theta_2 = \frac{2}{3}\pi, \qquad \theta_3 = \frac{4}{3}\pi. \tag{A.1}$$

Their wave vectors are explicitly given by

$$\boldsymbol{k}_1 = k_L \begin{pmatrix} 1 \\ 0 \end{pmatrix}, \quad \boldsymbol{k}_2 = \frac{k_L}{2} \begin{pmatrix} -1 \\ \sqrt{3} \end{pmatrix}, \quad \boldsymbol{k}_3 = -\frac{k_L}{2} \begin{pmatrix} 1 \\ \sqrt{3} \end{pmatrix}, \tag{A.2}$$

leading to the reciprocal-lattice basis vectors

$$\boldsymbol{b}_1 = \frac{k_L}{2} \begin{pmatrix} 3 \\ -\sqrt{3} \end{pmatrix}, \quad \boldsymbol{b}_2 = k_L \begin{pmatrix} 0 \\ \sqrt{3} \end{pmatrix}. \tag{A.3}$$

The primitive direct-lattice vectors follow through the relation $\boldsymbol{a}_i \cdot \boldsymbol{b}_j = 2\pi\delta_{i,j}$

$$\boldsymbol{a}_1 = \frac{\lambda_L}{3} \begin{pmatrix} 2 \\ 0 \end{pmatrix}, \quad \boldsymbol{a}_2 = \frac{\lambda_L}{3} \begin{pmatrix} 1 \\ \sqrt{3} \end{pmatrix}, \tag{A.4}$$

implying a lattice spacing of $a = 2\lambda_L/3$.

The diagonal matrix elements of the single-particle Hamiltonian for this potential can be obtained by evaluating Eq. (3.8)

$$\left\langle \boldsymbol{k} + \boldsymbol{G}_{l,p} \right| H_1 \left| \boldsymbol{k} + \boldsymbol{G}_{l,p} \right\rangle = E_R \left[\left(\frac{k_x}{k_L} + \frac{3}{2} l \right)^2 + \left(\frac{k_y}{k_L} - \frac{\sqrt{3}}{2} l + \sqrt{3} p \right)^2 \right]. \tag{A.5}$$

Figure A.1 (a) shows the resulting bandstructure up to the fourth excited band and Fig. 3.1 (a) shows the bandstructure along high symmetry directions

$$\boldsymbol{\Gamma} = \begin{pmatrix} 0 \\ 0 \end{pmatrix}, \quad \boldsymbol{M} = \frac{k_L}{4} \begin{pmatrix} 3 \\ \sqrt{3} \end{pmatrix} \text{ and } \boldsymbol{K} = k_L \begin{pmatrix} 1 \\ 0 \end{pmatrix}. \tag{A.6}$$

The directional derivative (in the k_x-direction) of the lowest band, which is also needed to evaluate Eq. (2.23), is shown in Fig. A.1 (b).

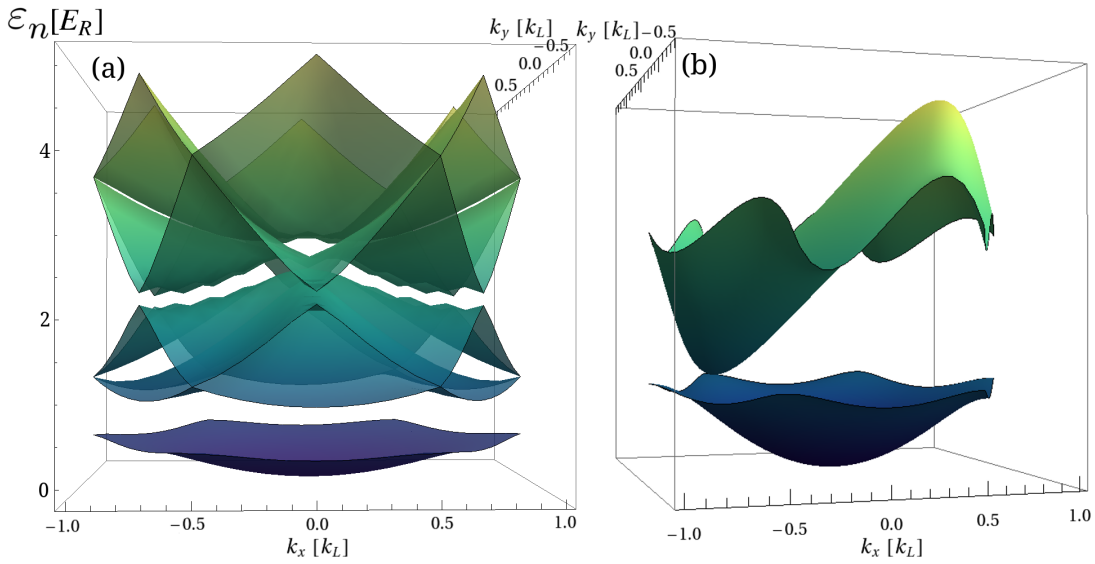

Figure A.1: (a) Numerically calculated band structure including the lowest five bands for the 3BTL with a light-shift strength parameter $V_0/E_R = -1$. (b) Lowest band (below) together with its derivative with respect to k_x (above) for $V_0/E_R = -1$. The scale is chosen arbitrary and different for both curves in order to visualize them more clearly.

A.2 The three-beam square lattice

A 3BSL is created by the angles

$$\theta_1 = \frac{\pi}{4}, \qquad \theta_2 = \frac{3\pi}{4}, \qquad \theta_3 = \frac{5\pi}{4}. \tag{A.7}$$

Their wave vectors are explicitly given by

$$\boldsymbol{k}_1 = k_L \begin{pmatrix} 1 \\ 1 \end{pmatrix}, \quad \boldsymbol{k}_2 = k_L \begin{pmatrix} -1 \\ 1 \end{pmatrix}, \quad \boldsymbol{k}_3 = -\boldsymbol{k}_1, \tag{A.8}$$

leading to the reciprocal-lattice basis vectors

$$\boldsymbol{b}_1 = \sqrt{2} k_L \begin{pmatrix} 1 \\ 0 \end{pmatrix}, \quad \boldsymbol{b}_2 = \sqrt{2} k_L \begin{pmatrix} 0 \\ 1 \end{pmatrix}. \tag{A.9}$$

The primitive direct-lattice vectors follow through the relation $\boldsymbol{a}_i \cdot \boldsymbol{b}_j = 2\pi\delta_{i,j}$

$$\boldsymbol{a}_1 = \frac{\lambda_L}{\sqrt{2}} \begin{pmatrix} 1 \\ 0 \end{pmatrix}, \quad \boldsymbol{a}_2 = \frac{\lambda_L}{\sqrt{2}} \begin{pmatrix} 0 \\ 1 \end{pmatrix}, \tag{A.10}$$

implying a lattice spacing of $a = \lambda_L/\sqrt{2}$.

The diagonal matrix elements of the single-particle Hamiltonian for this potential can be obtained by evaluating Eq. (3.8)

$$\left\langle \boldsymbol{k} + \boldsymbol{G}_{l,p} \right| H_1 \left| \boldsymbol{k} + \boldsymbol{G}_{l,p} \right\rangle = E_R \left[\left(\frac{k_x}{k_L} + \sqrt{2} l \right)^2 + \left(\frac{k_y}{k_L} + \sqrt{2} p \right)^2 \right]. \tag{A.11}$$

Figure 3.1 (b) shows the bandstructure along high symmetry directions

$$\boldsymbol{\Gamma} = \begin{pmatrix} 0 \\ 0 \end{pmatrix}, \quad \boldsymbol{M} = \frac{k_L}{\sqrt{2}} \begin{pmatrix} 1 \\ 1 \end{pmatrix} \text{ and } \boldsymbol{X} = \frac{k_L}{\sqrt{2}} \begin{pmatrix} 1 \\ 0 \end{pmatrix}. \tag{A.12}$$

A.3 The four-beam square lattice

The 4BSL is created by four lasers beams mutually enclosing angles of $\pi/2$. This setup leads to the reciprocal-lattice basis vectors

$$\boldsymbol{b}_1 = 2k_L \begin{pmatrix} 1 \\ 0 \end{pmatrix}, \quad \boldsymbol{b}_2 = 2k_L \begin{pmatrix} 0 \\ 1 \end{pmatrix}. \tag{A.13}$$

The primitive direct-lattice vectors follow through the relation $\boldsymbol{a}_i \cdot \boldsymbol{b}_j = 2\pi\delta_{i,j}$

$$\boldsymbol{a}_1 = \frac{\lambda_L}{2} \begin{pmatrix} 1 \\ 0 \end{pmatrix}, \quad \boldsymbol{a}_2 = \frac{\lambda_L}{2} \begin{pmatrix} 0 \\ 1 \end{pmatrix}, \tag{A.14}$$

implying a lattice spacing of $a = \lambda_L/2$.

The diagonal matrix elements of the single-particle Hamiltonian for this potential can be obtained by evaluating Eq. (3.8)

$$\langle \boldsymbol{k} + \boldsymbol{G}_{l,p} | \, H_1 \, | \boldsymbol{k} + \boldsymbol{G}_{l,p} \rangle = E_R \left[\left(\frac{k_x}{k_L} + 2l \right)^2 + \left(\frac{k_y}{k_L} + 2p \right)^2 \right]. \tag{A.15}$$

Figure 3.1 (c) shows the bandstructure along high symmetry directions

$$\boldsymbol{\Gamma} = \begin{pmatrix} 0 \\ 0 \end{pmatrix}, \quad \boldsymbol{M} = k_L \begin{pmatrix} 1 \\ 1 \end{pmatrix} \text{ and } \boldsymbol{X} = k_L \begin{pmatrix} 1 \\ 0 \end{pmatrix}. \tag{A.16}$$

Appendix B

Auxiliary calculations for the derivation of the superfluid-drag coefficient

B.1 Transformation from real space to momentum space

Inserting the relation (2.1) into the Hamiltonian given by Eq. (1.38) yields

$$\begin{aligned} H = &\frac{1}{N}\sum_{ij,\alpha}\sum_{\boldsymbol{k},\boldsymbol{q}} J_{ij\alpha} e^{i(\boldsymbol{k}\boldsymbol{r}_i - \boldsymbol{q}\boldsymbol{r}_j)} b^\dagger_{\boldsymbol{k}\alpha} b_{\boldsymbol{q}\alpha} \\ &+ \frac{1}{2N^2}\sum_{i,\alpha\beta} U_{\alpha\beta} \sum_{\boldsymbol{k}_1\ldots\boldsymbol{k}_4} e^{i(\boldsymbol{k}_1+\boldsymbol{k}_2-\boldsymbol{k}_3-\boldsymbol{k}_4)\boldsymbol{r}_i} b^\dagger_{\boldsymbol{k}_1\alpha} b^\dagger_{\boldsymbol{k}_2\beta} b_{\boldsymbol{k}_3\beta} b_{\boldsymbol{k}_4\alpha} \,. \end{aligned} \tag{B.1}$$

In a system with discrete translational invariance, $J_{ij\alpha}$ can only depend on the difference $\boldsymbol{\rho} = \boldsymbol{r}_i - \boldsymbol{r}_j$ and not on the individual lattice sites. The Hamiltonian can therefore be rewritten in the following way

$$\begin{aligned} H = &\sum_{\boldsymbol{k},\alpha}\sum_{\boldsymbol{q},\boldsymbol{\rho}} J_{\boldsymbol{\rho}\alpha} e^{i\boldsymbol{q}\boldsymbol{\rho}} \frac{1}{N}\sum_i e^{i(\boldsymbol{k}-\boldsymbol{q})\boldsymbol{r}_i} b^\dagger_{\boldsymbol{k}\alpha} b_{\boldsymbol{q}\alpha} \\ &+ \frac{1}{2N^2}\sum_{i,\alpha\beta} U_{\alpha\beta} \sum_{\boldsymbol{k}_1\ldots\boldsymbol{k}_4} e^{i(\boldsymbol{k}_1+\boldsymbol{k}_2-\boldsymbol{k}_3-\boldsymbol{k}_4)\boldsymbol{r}_i} b^\dagger_{\boldsymbol{k}_1\alpha} b^\dagger_{\boldsymbol{k}_2\beta} b_{\boldsymbol{k}_3\beta} b_{\boldsymbol{k}_4\alpha} \,. \end{aligned} \tag{B.2}$$

Using the identity

$$\frac{1}{N}\sum_i e^{i\boldsymbol{k}\boldsymbol{r}_i} = \delta_{\boldsymbol{k},0}, \tag{B.3}$$

the Hamiltonian can be brought into the form of Eq. (2.2):

$$H = \sum_{\boldsymbol{k},\alpha} \underbrace{\sum_{\boldsymbol{\rho}} J_{\boldsymbol{\rho}\alpha} e^{i\boldsymbol{k}\boldsymbol{\rho}}}_{\varepsilon_{\boldsymbol{k}\alpha}} b^\dagger_{\boldsymbol{k}\alpha} b_{\boldsymbol{k}\alpha} + \frac{1}{2N}\sum_{\alpha\beta} U_{\alpha\beta} \sum_{\boldsymbol{k}_1\ldots\boldsymbol{k}_4} b^\dagger_{\boldsymbol{k}_1\alpha} b^\dagger_{\boldsymbol{k}_2\beta} b_{\boldsymbol{k}_3\beta} b_{\boldsymbol{k}_4\alpha} \delta_{\boldsymbol{k}_1+\boldsymbol{k}_2,\boldsymbol{k}_3+\boldsymbol{k}_4} \,. \tag{B.4}$$

B.2 Application of the Bogoliubov approximation

In order to derive the Hamiltonian in Eq. (2.4) from Eq. (B.4), we bring the interaction term into bilinear form and pull the ground state ($\boldsymbol{k} = 0$) out of the sum over $\boldsymbol{k}$. The kinetic part of the Hamiltonian is already bilinear so we only separate the $\boldsymbol{k} = 0$ state from the sum:

$$\begin{aligned} H_{\text{kin}} &= \sum_{\boldsymbol{k},\alpha} \varepsilon_{\boldsymbol{k}\alpha} b^\dagger_{\boldsymbol{k}\alpha} b_{\boldsymbol{k}\alpha} \\ &= \sum_{\alpha} \left[\varepsilon_{0\alpha} N_{0\alpha} + {\sum_{\boldsymbol{k}}}' \varepsilon_{\boldsymbol{k}\alpha} b^\dagger_{\boldsymbol{k}\alpha} b_{\boldsymbol{k}\alpha} \right] \\ &= \sum_{\alpha} \left[\varepsilon_{0\alpha} N_{\alpha} + {\sum_{\boldsymbol{k}}}' (\varepsilon_{\boldsymbol{k}\alpha} - \varepsilon_{0\alpha}) b^\dagger_{\boldsymbol{k}\alpha} b_{\boldsymbol{k}\alpha} \right], \end{aligned} \tag{B.5}$$

where we used the relation

$$N_{0\alpha} = N_\alpha - {\sum_{\boldsymbol{k}}}' b^\dagger_{\boldsymbol{k}\alpha} b_{\boldsymbol{k}\alpha} \,. \tag{B.6}$$

The interaction term is a little bit more complicated. We use the Bogoliubov approximation, Eq. (2.3), and only keep the bilinear terms. Taking into account the Kronecker delta we are then left with the terms:

1. $\{\boldsymbol{k}_i\} = 0$
2. $\boldsymbol{k}_1 = 0,\ \boldsymbol{k}_2 = \boldsymbol{k},\ \boldsymbol{k}_3 = 0,\ \boldsymbol{k}_4 = \boldsymbol{k}$
3. $\boldsymbol{k}_1 = \boldsymbol{k},\ \boldsymbol{k}_2 = 0,\ \boldsymbol{k}_3 = \boldsymbol{k},\ \boldsymbol{k}_4 = 0$
4. $\boldsymbol{k}_1 = 0,\ \boldsymbol{k}_2 = \boldsymbol{k},\ \boldsymbol{k}_3 = \boldsymbol{k},\ \boldsymbol{k}_4 = 0$
5. $\boldsymbol{k}_1 = \boldsymbol{k},\ \boldsymbol{k}_2 = 0,\ \boldsymbol{k}_3 = 0,\ \boldsymbol{k}_4 = \boldsymbol{k}$
6. $\boldsymbol{k}_1 = \boldsymbol{k},\ \boldsymbol{k}_2 = -\boldsymbol{k},\ \boldsymbol{k}_3 = 0,\ \boldsymbol{k}_4 = 0$
7. $\boldsymbol{k}_1 = 0,\ \boldsymbol{k}_2 = 0,\ \boldsymbol{k}_3 = \boldsymbol{k},\ \boldsymbol{k}_4 = -\boldsymbol{k}$

Inserting these allowed combinations for $\boldsymbol{k}$ into the interaction part of the Hamiltonian leads to

$$
\begin{aligned}
H_{\text{int}} &= \frac{1}{2N}\sum_{\alpha\beta}U_{\alpha\beta}\sum_{\boldsymbol{k}_1\ldots\boldsymbol{k}_4} b^\dagger_{\boldsymbol{k}_1\alpha}b^\dagger_{\boldsymbol{k}_2\beta}b_{\boldsymbol{k}_3\beta}b_{\boldsymbol{k}_4\alpha}\delta_{\boldsymbol{k}_1+\boldsymbol{k}_2,\boldsymbol{k}_3+\boldsymbol{k}_4} \\
&= \frac{1}{2N}\sum_{\alpha\beta}U_{\alpha\beta}\Bigg\{N_{0\alpha}N_{0\beta} + {\sum_{\boldsymbol{k}}}'\Big[N_{0\alpha}b^\dagger_{\boldsymbol{k}\beta}b_{\boldsymbol{k}\beta} + N_{0\beta}b^\dagger_{\boldsymbol{k}\alpha}b_{\boldsymbol{k}\alpha} + \\
&\qquad \sqrt{N_{0\alpha}N_{0\beta}}\left(b^\dagger_{\boldsymbol{k}\beta}b_{\boldsymbol{k}\alpha} + b^\dagger_{\boldsymbol{k}\alpha}b_{\boldsymbol{k}\beta} + b_{\boldsymbol{k}\beta}b_{-\boldsymbol{k}\alpha} + b^\dagger_{\boldsymbol{k}\alpha}b^\dagger_{-\boldsymbol{k}\beta}\right)\Big]\Bigg\} \qquad \text{(B.7)} \\
&= \frac{N_AN_B}{N}U_{AB} + \sum_\alpha\left(\frac{N_\alpha^2}{2N}U_\alpha\right) + {\sum_{\boldsymbol{k}}}'\Bigg\{\sqrt{n_An_B}\,U_{AB}\Big(b^\dagger_{\boldsymbol{k}A}b_{\boldsymbol{k}B} + b^\dagger_{\boldsymbol{k}B}b_{\boldsymbol{k}A} + \\
&\quad b_{\boldsymbol{k}B}b_{-\boldsymbol{k}A} + b^\dagger_{\boldsymbol{k}A}b^\dagger_{-\boldsymbol{k}B}\Big) + \sum_\alpha\left[\frac{n_\alpha}{2}U_\alpha\left(2b^\dagger_{\boldsymbol{k}\alpha}b_{\boldsymbol{k}\alpha} + b_{\boldsymbol{k}\alpha}b_{-\boldsymbol{k}\alpha} + b^\dagger_{\boldsymbol{k}\alpha}b^\dagger_{-\boldsymbol{k}\alpha}\right)\right]\Bigg\}.
\end{aligned}
$$

For the last equality we used relation (B.6) and only kept the parts bilinear in the creation/annihilation operators. $H = H_{\text{kin}} + H_{\text{int}}$ now directly leads to the Hamiltonian given by Eq. (2.4).

B.3 Expansion of the excitation spectrum

The aim of this Appendix is to find an expression for the free energy, Eq. (2.19), up to bilinear order in the superfluid velocities by expanding $\mathcal{E}_{\boldsymbol{k}\sigma}$. Under the transformation given in Eq. (2.22), the matrix $\mathcal{M}_{\boldsymbol{k}}$ adopts the form

$$
\mathcal{M}_{\boldsymbol{k}} = \begin{pmatrix} E^A_{\boldsymbol{k}} - s^A_{\boldsymbol{k}} & F_{AB} & F_A & F_{AB} \\ F_{AB} & E^B_{\boldsymbol{k}} - s^B_{\boldsymbol{k}} & F_{AB} & F_B \\ F_A & F_{AB} & E^A_{\boldsymbol{k}} + s^A_{\boldsymbol{k}} & F_{AB} \\ F_{AB} & F_B & F_{AB} & E^B_{\boldsymbol{k}} + s^B_{\boldsymbol{k}} \end{pmatrix}, \qquad \text{(B.8)}
$$

where $s^\alpha_{\boldsymbol{k}} = m_\alpha \boldsymbol{v}_{s\alpha}\cdot\boldsymbol{\nabla}_{\boldsymbol{k}}\epsilon^\alpha_{\boldsymbol{k}}$, $F_\alpha = n_\alpha U_\alpha$, $F_{AB} = \sqrt{n_An_B}\,U_{AB}$, $E^\alpha_{\boldsymbol{k}} = \epsilon^\alpha_{\boldsymbol{k}} + F_\alpha$ and $\epsilon^\alpha_{\boldsymbol{k}} = \varepsilon_{\boldsymbol{k}\alpha} - \varepsilon_{0\alpha}$. Furthermore we made use of the fact that $E^\alpha_{\boldsymbol{k}} = E^\alpha_{-\boldsymbol{k}}$ and $s^\alpha_{\boldsymbol{k}} = -s^\alpha_{-\boldsymbol{k}}$ (because the nabla operator is linear in $\boldsymbol{k}$). The characteristic polynomial which defines $\mathcal{E}_{\boldsymbol{k}\sigma}$ is given by

$$
|\mathcal{M}_{\boldsymbol{k}}\sigma_3 - \mathcal{E}_{\boldsymbol{k}}\mathbb{1}_4| = 0. \qquad \text{(B.9)}
$$

As a next step we expand the characteristic polynomial in powers of $s^\alpha_{\boldsymbol{k}}$, using the notation

$$
\mathcal{E}_{\boldsymbol{k}} = \mathcal{E}^0_{\boldsymbol{k}} + \mathcal{E}^1_{\boldsymbol{k}} + \mathcal{E}^2_{\boldsymbol{k}} + \mathcal{O}([s^\alpha_{\boldsymbol{k}}]^2), \qquad \text{(B.10)}
$$

where the superscript denotes the order in $s^\alpha_{\boldsymbol{k}}$ and order two means bilinear. The resulting equation in zeroth order leads to the excitation spectrum in the absence of

superfluid velocities, Eq. (2.16). The terms linear in $s^\alpha_{\boldsymbol{k}}$ result in

$$\mathcal{E}^1_{\boldsymbol{k}\sigma} = \frac{\epsilon^B_{\boldsymbol{k}}\left(\epsilon^B_{\boldsymbol{k}}+2F_B\right)-\epsilon^A_{\boldsymbol{k}}\left(\epsilon^A_{\boldsymbol{k}}+2F_A\right)-\sigma\left[\left(\mathcal{E}^0_{\boldsymbol{k}+}\right)^2+\left(\mathcal{E}^0_{\boldsymbol{k}-}\right)^2\right]}{2\sigma\left[\left(\mathcal{E}^0_{\boldsymbol{k}+}\right)^2+\left(\mathcal{E}^0_{\boldsymbol{k}-}\right)^2\right]} s^A_{\boldsymbol{k}} + \left[A\leftrightarrow B\right], \tag{B.11}$$

and the bilinear part of the spectrum reads

$$\mathcal{E}^2_{\boldsymbol{k}\sigma} = \left[\frac{\left(\mathcal{E}^0_{\boldsymbol{k}+}\right)^2-\left(\mathcal{E}^0_{\boldsymbol{k}-}\right)^2}{\mathcal{E}^0_{\boldsymbol{k}\sigma}} - 4\sigma\mathcal{E}^0_{\boldsymbol{k}\sigma}\right]\frac{4F^2_{AB}\epsilon^A_{\boldsymbol{k}}\epsilon^B_{\boldsymbol{k}}}{\left[\left(\mathcal{E}^0_{\boldsymbol{k}+}\right)^2-\left(\mathcal{E}^0_{\boldsymbol{k}-}\right)^2\right]^3} s^A_{\boldsymbol{k}}s^B_{\boldsymbol{k}}. \tag{B.12}$$

All linear terms in $s^\alpha_{\boldsymbol{k}}$ cancel under the sum of Eq. (2.19) because $s^\alpha_{\boldsymbol{k}}$ is an odd function of $\boldsymbol{k}$. Additionally all the terms independent of $s^\alpha_{\boldsymbol{k}}$ are comprised by the F_0 term. We therefore only have to consider terms bilinear in the superfluid velocities. Inserting Eq. (B.12) in the free energy, we obtain

$$F_{T=0} = F_0 + 2{\sum_{\boldsymbol{k}}}' \frac{F^2_{AB}\epsilon^A_{\boldsymbol{k}}\epsilon^B_{\boldsymbol{k}}}{\mathcal{E}^0_{\boldsymbol{k}+}\mathcal{E}^0_{\boldsymbol{k}-}\left[\mathcal{E}^0_{\boldsymbol{k}+}+\mathcal{E}^0_{\boldsymbol{k}-}\right]^3} s^A_{\boldsymbol{k}}s^B_{\boldsymbol{k}} + \mathcal{O}([s^\alpha_{\boldsymbol{k}}]^2). \tag{B.13}$$

If we assume that the the two velocities are parallel to each other (e.g., in the direction of one of the lattice vectors), we can use $s^\alpha_{\boldsymbol{k}} = m_\alpha\left(\partial_{k_u}\epsilon^\alpha_{\boldsymbol{k}}\right)v_{s\alpha}$ to rewrite the free energy

$$F_{T=0} = F_0 + 2{\sum_{\boldsymbol{k}}}' \frac{m_A m_B F^2_{AB}\epsilon^A_{\boldsymbol{k}}\epsilon^B_{\boldsymbol{k}}}{\mathcal{E}^0_{\boldsymbol{k}+}\mathcal{E}^0_{\boldsymbol{k}-}\left[\mathcal{E}^0_{\boldsymbol{k}+}+\mathcal{E}^0_{\boldsymbol{k}-}\right]^3}\left(\partial_{k_u}\epsilon^A_{\boldsymbol{k}}\right)\left(\partial_{k_u}\epsilon^B_{\boldsymbol{k}}\right)v_{sA}v_{sB} + \mathcal{O}(v^2_{s\alpha}). \tag{B.14}$$

Comparing this equation to Eq. (1.20), one can directly read off the superfluid-drag coefficient given in Eq. (2.23).

Appendix C

Numerical considerations

C.1 Discretization of the first Brillouin zone

In order to evaluate sums and integrals in $\boldsymbol{k}$-space and to calculate the bandstructures, Fig. 3.1, the first Brillouin zone (BZ) of the respective lattice is represented by a mesh of discrete points. For evaluating the directional derivative of the lowest band, Fig. A.1 (b), points outside the BZ were included in the mesh in order to be able to apply the symmetrized derivative at all relevant $\boldsymbol{k}$-points

$$\frac{\partial E(k_x, k_y)}{\partial k_x} \approx \frac{E(k_x + \Delta k, k_y) - E(k_x - \Delta k, k_y)}{2\Delta k}. \tag{C.1}$$

Discrete values of $\boldsymbol{k}$ imply boundary conditions in real space. Our discretization is chosen to fill out the BZ in a uniform way and to exhibit the symmetry of the respective lattice (see Fig. C.1 for the 3BTL). For the 3BTL, this does not correspond to the quantization which is expected by applying periodic boundary conditions given by

$$\frac{k_x}{k_L} = \frac{3l}{2\sqrt{N}}, \qquad \frac{k_y}{k_L} = \sqrt{\frac{3}{N}}\left(p - \frac{l}{2}\right), \qquad l, p \in \mathbb{Z}. \tag{C.2}$$

For an infinitely large lattice, the mesh should become infinitely dense and all results should be independent of the boundary conditions. By making our mesh sufficiently dense and the volume we use for the integrals sufficiently large, we thus expect our numerical results to give reasonable values. However, it may well be that our results could be improved by creating a mesh which satisfies Eq. (C.2) and using a consistent volume as "all space".

C.2 Numerics and units

When doing numerical calculations, one obviously needs to work with unitless numbers. It is therefore important to keep track of the units, such that the output of the calculation, a bare number, is interpreted correctly. In general, we express all energies in units of the recoil energy of component A, all reciprocal-space vectors in units of

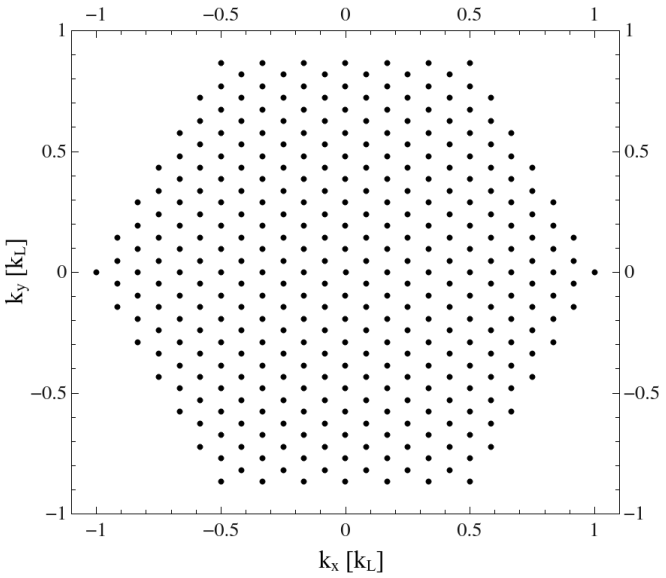

Figure C.1: Discretization of the first BZ for the 3BTL. The mesh is chosen to have a homogeneous density and to respect the symmetry of the optical lattice.

the magnitude of the laser wave vector k_L and all real-space vectors in units of its wavelength λ_L.

C.2.1 Wannier functions

Using Eqs. (3.2, 3.12), the Wannier function centered at the origin can be written as

$$W(\boldsymbol{r}) = \frac{1}{\sqrt{\mathcal{V}N}} \sum_{\boldsymbol{k}} e^{i\boldsymbol{k}\cdot\boldsymbol{r}} u_{\boldsymbol{k}}(\boldsymbol{r}). \tag{C.3}$$

A volume that is consistent with there being N allowed $\boldsymbol{k}$ values is

$$\mathcal{V} = N\mathcal{V}_{\mathrm{WS}}, \tag{C.4}$$

where $\mathcal{V}_{\mathrm{WS}}$ is the volume of the Wigner-Seitz cell. For definiteness lets consider the 3BTL, where

$$\begin{aligned} \mathcal{V}_{\mathrm{WS}} &= \frac{2}{3\sqrt{3}}\lambda_L^2, \\ \Rightarrow W(\boldsymbol{r}) &= \frac{1}{\lambda_L N}\sqrt{\frac{3\sqrt{3}}{2}} \sum_{\boldsymbol{k}} e^{i\boldsymbol{k}\cdot\boldsymbol{r}} u_{\boldsymbol{k}}(\boldsymbol{r}). \end{aligned} \tag{C.5}$$

Since one usually does not want to define λ_L at this stage, the quantity that is calculated numerically is $W(\boldsymbol{r}) \cdot \lambda_L$ (that is why the absolute square of the Wannier functions in Fig. 3.2 is given in units of λ_L^{-2}).

C.2.2 Integrals

When evaluating integrals numerically, the integration over some volume is replaced by a discrete sum

$$\int_{\mathcal{V}} dx\, dy \quad \rightarrow \quad \sum_{\#} \Delta x \Delta y, \tag{C.6}$$

where # is the number of summands. Again choosing the volume of integration to be N times the Wigner-Seitz cell, we replace the finite element $\Delta x \Delta y$ and obtain

$$\begin{aligned} \Delta x \Delta y &= \frac{\mathcal{V}}{\#} = \frac{N\mathcal{V}_{\mathrm{WS}}}{\#}, \\ \Rightarrow \int_{\mathcal{V}} dx\, dy \quad &\rightarrow \quad \frac{N\mathcal{V}_{\mathrm{WS}}}{\#} \sum_{\#}. \end{aligned} \tag{C.7}$$

Since the Wigner-Seitz cell is proportional to λ_L^2 for all lattices, we always divide the integral by this factor before evaluating it. When performing an integration over the absolute value squared of a Wannier function, the factors λ_L cancel out and the result does not depend on the laser wavelength. However, for the Hubbard-interaction parameters, where Wannier functions to the power of four are involved, Eq. (1.39), the result is proportional to λ_L^2.

C.2.3 Derivatives

When evaluating the numerical derivative, Eq. (C.1), we want to express k_x, k_y and Δk all in units of k_L. Since the energy only depends on $\boldsymbol{k}/k_L$ [cf. Eqs. (A.5, A.11, A.15)], this only matters for the denominator and implies that we have to multiply the derivative with k_L before evaluating it if we do not want to specify k_L at this stage.

C.3 From component A to component B

For the numerical calculations, we want to express all the quantities in terms of the recoil energy of component A to have dimensionless quantities

$$E_R^A = \frac{k_L^2}{2m_A}, \quad E_R^B = E_R^A \frac{m_A}{m_B}. \tag{C.8}$$

If component A experiences the relative potential V_0/E_R^A, component B therefore feels the relative potential $V_0/E_R^A \times m_B/m_A$.

Examining its matrix elements, Eqs. (3.10, A.5, A.11, A.15), it can easily be verified that the single-particle Hamiltonian for all the lattices can be written as the recoil energy times an operator which only depends on the ratio V_0/E_R

$$H(V_0, E_R, \boldsymbol{k}) = E_R \cdot \tilde{H}(V_0/E_R, \boldsymbol{k}). \tag{C.9}$$

The eigenvalues of H are thus just the eigenvalues of $\tilde{H}$ times E_R, while the eigenstates of the two operators are the same. This leads to the following relations between the physical quantities and the numerically obtained ones

$$\begin{aligned} \frac{\varepsilon^A_{\boldsymbol{k}}}{E^A_R} &= \tilde{\varepsilon}_{\boldsymbol{k}}\left(\tfrac{V_0}{E^A_R}\right), \quad \frac{\varepsilon^B_{\boldsymbol{k}}}{E^A_R} = \frac{m_A}{m_B}\tilde{\varepsilon}_{\boldsymbol{k}}\left(\tfrac{m_B}{m_A}\tfrac{V_0}{E^A_R}\right), \\ W_A &= \tilde{W}\left(\tfrac{V_0}{E^A_R}\right), \quad W_B = \tilde{W}\left(\tfrac{m_B}{m_A}\tfrac{V_0}{E^A_R}\right), \end{aligned} \tag{C.10}$$

where the quantities with a tilde are calculated using eigenvalues and eigenstates of $\tilde{H}$ and the arguments in brackets correspond to the variable V_0/E_R in Eq. (C.9) which should be used when solving $\tilde{H}$.

Appendix D

The quasi two-dimensional system

Imposing two-dimensionality by a deep one-dimensional optical lattice, as explained in the text, has an influence on both the bandstructure and the Hubbard-interaction parameters when going from the three-dimensional microscopic Hamiltonian, Eq. (1.33), to the two-dimensional lattice representation, Eq. (1.38).

The single particle Hamiltonian in three-dimensions is given by

$$H_1^{\mathrm{3D}} = H_1 - \frac{1}{2m}\frac{\partial^2}{\partial z^2} + V_z \sin^2(k_L z), \tag{D.1}$$

where H_1 is the single particle Hamiltonian in two dimensions, Eq. (3.1). Since the z-dependent terms of this Hamiltonian are separated from the $\boldsymbol{r} = (x, y)$-dependent terms, its eigenfunctions can be written as products and its eigenenergies as sums (omitting the band index)

$$\begin{aligned} \Psi_{\boldsymbol{k},k_z}(\boldsymbol{r}, z) &= \Psi_{\boldsymbol{k}}(\boldsymbol{r})\Psi_{k_z}(z), \\ \varepsilon_{\boldsymbol{k},k_z} &= \varepsilon_{\boldsymbol{k}} + \varepsilon_{k_z}. \end{aligned} \tag{D.2}$$

Because the dynamics in the z-direction are frozen, this leads to a constant offset in the bandstructure $\varepsilon_{k_z=0}$ which in general depends on the component mass. However, since the spectrum of the quasiparticles only depends on $\epsilon_{\boldsymbol{k},0} = \varepsilon_{\boldsymbol{k},0} - \varepsilon_{0,0} = \epsilon_{\boldsymbol{k}}$, this only affects the ground state energy and has no influence on the superfluid drag.

Equation (D.2) implies that also the Wannier functions can be written as a product, which leads to a modification of the Hubbard-interaction parameters as discussed in the text [cf. Eq. (3.17)].

Appendix E

Introducing the superfluid velocity via the order parameter

Fisher *et al.* [16] introduced a finite superfluid velocity by twisting the boundary conditions of the order parameter. It has not become completely clear to us how this is related to twisting the boundary conditions of the many-body wavefunction. When defining the order parameter through the single-particle wavefunction of Eq. (1.3), the two approaches are clearly not equivalent in the case of a finite depletion of the condensate. This can be illustrated for the simplified case of a two particle system with a one particle "condensate" and depletion. The "condensed" particle occupies the single-particle wavefunction which defines the order parameter while the remaining particle is in the state χ_1 which fulfills single valued boundary conditions

$$\begin{aligned} \psi_2(\boldsymbol{r}_1, \boldsymbol{r}_2) &\propto \left[\Psi(\boldsymbol{r}_1)\chi_1(\boldsymbol{r}_2) + \chi_1(\boldsymbol{r}_1)\Psi(\boldsymbol{r}_2)\right], \\ \Rightarrow \psi_2(\boldsymbol{r}_1 + L\hat{\boldsymbol{u}}, \boldsymbol{r}_2) &\propto \left[e^{-i\Delta\varphi}\Psi(\boldsymbol{r}_1)\chi_1(\boldsymbol{r}_2) + \chi_1(\boldsymbol{r}_1)\Psi(\boldsymbol{r}_2)\right]. \end{aligned} \tag{E.1}$$

If the order parameter is defined through the expectation value of the boson annihilation operator and if one expresses this operator in terms of a density and a phase operator [41], denoted here by a hat,

$$\psi(\boldsymbol{r}) = e^{i\hat{\phi}(\boldsymbol{r})}\sqrt{\hat{n}(\boldsymbol{r})}, \tag{E.2}$$

then twisting the boundary conditions of the order parameter twists the boundary conditions of the bosonic field operators and therefore of every single-particle state. In this case a twist in the boundary conditions of the order parameter corresponds to the same effect on the many-body wavefunction ψ_N. Note that the same does not hold for the more common definition

$$\psi(\boldsymbol{r}) = \Psi(\boldsymbol{r}) + \delta\hat{\psi}(\boldsymbol{r}), \tag{E.3}$$

where $\delta\hat{\psi}(\boldsymbol{r})$ is the operator for the fluctuations of the bose field operator around a mean value $\Psi(\boldsymbol{r})$.

Bibliography

[1] For a review, see, e.g., A. J. Leggett, "Bose-Einstein condensation in the alkali gases: some fundamental concepts," Rev. Mod. Phys. **73**, 307 (2001). 1, 1.3

[2] For a review, see, e.g., D. Jaksch and P. Zoller, "The cold atom Hubbard toolbox," Ann. Phys. (N.Y.) **315**, 52 (2005). 1, 1.4

[3] A. Andreev and E. Bashkin, "Three-velocity hydrodynamics of superfluid solutions," Zh. Eksp. Teor. Fiz. **69**, 319 (1975). 1, 1.2.2, 1.2.2

[4] D. V. Fil and S. I. Shevchenko, "Nondissipative drag of superflow in a two-component Bose gas," Phys. Rev. A **72**, 013616 (2005). 1

[5] J. Linder and A. Sudbø, "Calculation of drag and superfluid velocity from the microscopic parameters and excitation energies of a two-component Bose-Einstein condensate in an optical lattice," Phys. Rev. A **79**, 063610 (2009). 1, 2, 3, 4, 5

[6] Y. Yanay and E. J. Mueller, "Superfluid density of weakly interacting bosons on a lattice," preprint, **arXiv**:1209.2446 (2012). 1

[7] V. M. Kaurov, A. B. Kuklov, and A. E. Meyerovich, "Drag effect and topological complexes in strongly interacting two-component lattice superfluids," Phys. Rev. Lett. **95**, 090403 (2005). 1, 5

[8] P. B. Blakie and C. W. Clark, "Wannier states and Bose-Hubbard parameters for 2D optical lattices," J. Phys. B: At. Mol. Opt. Phys. **37**, 1391 (2004). 1, 1.4, 1.5, 1.4, 3.2

[9] C. Becker, P. Soltan-Panahi, J. Kronjäger, S. Dörscher, K. Bongs, and K. Sengstock, "Ultracold quantum gases in triangular optical lattices," New J. Phys. **12**, 065025 (2010). 1, 3.1, 3.2

[10] P. P. Hofer, C. Bruder, and V. M. Stojanović, "Superfluid drag of two-species Bose-Einstein condensates in optical lattices," Phys. Rev. A **86**, 033627 (2012). 1

[11] P. C. Hohenberg and P. C. Martin, "Microscopic theory of superfluid helium," Ann. Phys. (N.Y.) **34**, 291 (1965). 1.1.2

[12] A. J. Leggett, *Quantum liquids: Bose condensation and Cooper pairing in condensed-matter Systems* (Oxford University Press, New York, 2006). 1.1.2, 1.2.1, 1.2.1

[13] L. Landau, "Theory of the superfluidity of helium II," Phys. Rev. **60**, 356 (1941). 1.2.1

[14] A. J. Leggett, "Superfluidity," Rev. Mod. Phys. **71**, S318 (1999). 1.2.1, 1.2.1

[15] P. P. Hofer, "On the limits for the superfluid fraction of arbitrary many-body systems at T=0 derived by A. J. Leggett," M. S. Project, University of Basel (2011). 1.2.1

[16] M. E. Fisher, M. N. Barber, and D. Jasnow, "Helicity modulus, superfluidity, and scaling in isotropic systems," Phys. Rev. A **8**, 1111 (1973). 1.2.1, E

[17] H. J. Metcalf and P. van der Straten, *Laser cooling and trapping* (Springer, 1999). 1.3, 1.4

[18] I. Bloch, J. Dalibard, and W. Zwerger, "Many-body physics with ultracold gases," Rev. Mod. Phys. **80**, 885 (2008). 1.3

[19] C. Pethick and H. Smith, *Bose-Einstein condensation in dilute gases* (Cambridge University Press, 2008). 1.3, 1.2, 1.4, 2.1

[20] J. Weiner, V. S. Bagnato, S. Zilio, and P. S. Julienne, "Experiments and theory in cold and ultracold collisions," Rev. Mod. Phys. **71**, 1 (1999). 1.3

[21] P. Soltan-Panahi, J. Struck, P. Hauke, A. Bick, W. Plenkers, G. Meineke, C. Becker, P. Windpassinger, M. Lewenstein, and K. Sengstock, "Multi-component quantum gases in spin-dependent hexagonal lattices," Nat. Phys. **7**, 434 (2011). 1.4, 1.6

[22] J. Catani, L. De Sarlo, G. Barontini, F. Minardi, and M. Inguscio, "Degenerate Bose-Bose mixture in a three-dimensional optical lattice," Phys. Rev. A **77**, 011603(R) (2008). 1.4, 1.6

[23] D. Jaksch, C. Bruder, J. I. Cirac, C. Gardiner, and P. Zoller, "Cold bosonic atoms in optical lattices," Phys. Rev. Lett. **81**, 3108 (1998). 1.5

[24] W. Zwerger, "Many-body physics with ultracold gases,", University Lecture, EPFL (2012). 1.5

[25] N. R. Cooper and Z. Hadzibabic, "Measuring the superfluid fraction of an ultracold atomic gas," Phys. Rev. Lett. **104**, 030401 (2010). 1.6, 5

[26] G. Modugno, M. Modugno, F. Riboli, G. Roati, and M. Inguscio, "Two atomic species superfluid," Phys. Rev. Lett. **89**, 190404 (2002). 1.6

[27] A. Lercher, T. Takekoshi, M. Debatin, B. Schuster, R. Rameshan, F. Ferlaino, R. Grimm, and H. Nägerl, "Production of a dual-species Bose-Einstein condensate of Rb and Cs atoms," Eur. Phys. J. D **65**, 3 (2011). 1.6

[28] S. B. Papp, J. M. Pino, and C. E. Wieman, "Tunable miscibility in a dual-species Bose-Einstein condensate," Phys. Rev. Lett. **101**, 040402 (2008). 1.6

[29] G. Thalhammer, G. Barontini, L. D. Sarlo, J. Catani, F. Minardi, and M. Inguscio, "Double species Bose-Einstein condensate with tunable interspecies interactions," Phys. Rev. Lett. **100**, 210402 (2008). 1.6

[30] C. J. Myatt, E. A. Burt, R. W. Ghrist, E. A. Cornell, and C. E. Wieman, "Two overlapping Bose-Einstein condensates by sympathetic cooling," Phys. Rev. Lett. **78**, 586 (1997). 1.6

[31] D. M. Weld, P. Medley, H. Miyake, D. Hucul, D. E. Pritchard, and W. Ketterle, "Spin gradient thermometry for ultracold atoms in optical lattices," Phys. Rev. Lett. **103**, 245301 (2009). 1.6

[32] C. Tsallis, "Diagonalization methods for the general bilinear Hamiltonian of an assembly of bosons," J. Math. Phys. **19**, 277 (1978). 2.2

[33] E. Herland, "Theoretical studies of two-component interacting Bose-Einstein condensates," M. S. Thesis, NTNU (2008). 2.3

[34] B. S. Garbow, J. M. Boyle, J. J. Dongarra, and C. B. Moler, *Matrix eigensystem routines - EISPACK guide extension* (Springer, New York, 1977). 3.1

[35] W. Kohn, "Analytic properties of Bloch waves and Wannier functions," Phys. Rev. **115**, 809 (1959). 3.2

[36] J. D. Cloizeaux, "Analytical properties of n-dimensional energy bands and Wannier functions," Phys. Rev. **135**, A698 (1964). 3.2

[37] T. Bulovyatova, "Numerical methods of localization of Wannier functions in modeling of photonic crystals," Ph.D. thesis, KIT (2011). 3.2

[38] N. Marzari and D. Vanderbilt, "Maximally localized generalized Wannier functions for composite energy bands," Phys. Rev. B **56**, 12847 (1997). 3.2

[39] A. A. Mostofi, J. R. Yates, Y. Lee, I. Souza, D. Vanderbilt, and N. Marzari, "Wannier90: A tool for obtaining maximally-localised Wannier functions," Comput. Phys. Commun. **178**, 685 (2008). 3.2

[40] I. Schnell, G. Czycholl, and R. C. Albers, "Hubbard-U calculations for Cu from first-principle Wannier functions," Phys. Rev. B **65**, 075103 (2002). 3.2

[41] V. N. Popov, *Functional integrals in quantum field theory and statistical physics* (Reidel, Dordrecht, 1983). E

Philosophisch-Naturwissenschaftliche Fakultät
der Universität Basel
Dekanat

Erklärung zur wissenschaftlichen Redlichkeit
(beinhaltet Erklärung zu Plagiat und Betrug)

(bitte ankreuzen)
☐ Bachelorarbeit
☒ Masterarbeit

Titel der Arbeit *(Druckschrift)*:

Superfluid drag of two-species Bose-Einstein condensates in optical lattices

Name, Vorname *(Druckschrift)*: Hofer, Patrick

Matrikelnummer: 07-058-787

Hiermit erkläre ich, dass mir bei der Abfassung dieser Arbeit nur die darin angegebene Hilfe zuteil wurde und dass ich sie nur mit den in der Arbeit angegebenen Hilfsmitteln verfasst habe.

Ich habe sämtliche verwendeten Quellen erwähnt und gemäss anerkannten wissenschaftlichen Regeln zitiert.

Diese Erklärung wird ergänzt durch eine separat abgeschlossene Vereinbarung bezüglich der Veröffentlichung oder öffentlichen Zugänglichkeit dieser Arbeit.

☐ ja ☒ nein

Ort, Datum: Basel, 15.11.2012

Unterschrift: P. Hofer